

## Review Article

## Coupled analysis of hydrogen diffusion, deformation, and fracture: a review

Alok Negi <sup>a,\*</sup>, Mohamed Elkhodibia <sup>a</sup>, Imad Barsoum <sup>a,b,\*</sup>, Akram AlFantazi <sup>c</sup><sup>a</sup> Department of Mechanical and Nuclear Engineering, Khalifa University of Science and Technology, Abu Dhabi, 127788, United Arab Emirates<sup>b</sup> Department of Engineering Mechanics, Royal Institute of Technology – KTH, Teknikringen 8, Stockholm, 100 44, Sweden<sup>c</sup> Department of Chemical and Petroleum Engineering, Khalifa University of Science and Technology, Abu Dhabi, 127788, United Arab Emirates

## ARTICLE INFO

## ABSTRACT

## Keywords:

Hydrogen embrittlement  
Hydrogen diffusion  
Dislocations  
Hydrogen-assisted cracking  
Fracture models  
Finite element analysis

Hydrogen (H), emerging as a sustainable and promising clean energy source, holds significant potential for transitioning towards a H-based economy, offering a cleaner alternative to traditional fossil fuels. However, hydrogen embrittlement (HE) poses a substantial obstacle to this transition, impacting critical sectors such as transportation, defense, energy production, and construction. Computational modeling, driven by the continuous development of new algorithms and high-performance computing platforms, emerges as an attractive avenue to unravel and address the complexities associated with HE. In particular, a multidisciplinary modeling approach shows potential in investigating the intricate interactions between H and materials across different temporal and spatial scales. Over the last few decades, there have already been many developments in computational modeling investigations based on a coupled study of H diffusion, deformation, and fracture processes to address multifaceted aspects of the HE problem. This comprehensive review sheds light on these advancements, providing insights into the modeling methodologies adopted in these investigations and their results. The review begins with a concise overview of commonly adopted mechanisms to explain HE. Thereafter, the discussion shifts to various advancements in H diffusion modeling, from early works to most recent developments, encompassing diverse aspects, such as H uptake and diffusion through the lattice structure and the role of microstructural traps and material microstructure. The last section of the review focuses on several theoretical and numerical studies that simulate how H affects the fracture characteristics and mechanical properties of various metals and alloys. This discussion includes applications of various state-of-the-art fracture models to predict H-assisted crack growth, as well as a range of theoretical models, continuum-based finite element simulations, and micro-meso scale modeling studies.

## 1. Introduction

Hydrogen (H), with its distinctive properties, has emerged as a promising and eco-friendly energy carrier, positioned as a viable alternative to conventional fossil fuels. In addition, switching to H as an energy source can help with environmental issues like lowering CO<sub>2</sub> emissions and battling climate change, paving the way for a future with no carbon emissions [1]. However, this transition faces a major obstacle in the form of hydrogen embrittlement (HE). Due to its small atomic size, H readily dissolves in various metals and alloys when exposed to various sources, such as air [2,3], aqueous solutions [4,5], soil [6,7], hydrocarbons in pipelines [8,9], and various chemically aggressive environments [10]. Once dissolved, its interactions with features within the crystal lattice of metals and alloys induce a transition from ductile-to-brittle material behavior, marked by a substantial reduction in strength, ductility, fracture toughness,

and fatigue resistance [3,11–13]. For example, it has been found in various experimental studies that the mechanical properties of steels suffer a significant drop with increasing H concentration [13–15]. Furthermore, various factors, including temperature, humidity, and deformation kinetics (e.g., strain rate or fatigue frequency), can also influence HE, making it a formidable concern across various industrial applications, such as aerospace, automotive, construction, and energy sectors [16,17].

Since its first report in 1874 [4] in a study on iron and steel fracture properties due to immersion in acids, a vast amount of work has been done to study HE in terms of both experimental and computational studies. Different mechanisms or models, such as H-enhanced decohesion (HEDE), H-enhanced localized plasticity (HELP), adsorption-induced dislocation emission (AIDE), and H-enhanced strain-induced vacancies (HESIV), have been proposed to explain HE. While these

\* Correspondence to: Department of Mechanical and Nuclear Engineering, School of Engineering, Khalifa University of Science and Technology, Abu Dhabi, 127788, United Arab Emirates.

E-mail addresses: [alok.negi@ku.ac.ae](mailto:alok.negi@ku.ac.ae) (A. Negi), [imad.barsoum@ku.ac.ae](mailto:imad.barsoum@ku.ac.ae) (I. Barsoum).

individual mechanisms offer valuable insights, it is increasingly recognized that a single mechanism alone cannot comprehensively describe all HE aspects [18,19]. Reasonable interpretations often involve a combination of mechanisms, such as HEDE and HELP [13,20,21], or new concepts such as nanovoid coalescence (NVC) [22]. Despite these developments, a complete understanding of the fundamental mechanism to explain HE is still incomplete due to various constraints, and the aim to comprehensively understand how H alters the properties of metal and alloys through intricate H-metal interactions across multiple time and length scales is still an active research problem.

Beyond various proposed mechanisms to explain HE, significant progress has also been made in recent years in the computational modeling to study the dynamic interplay between H and various microstructural features in metals/alloys and the resulting degradation of material properties, with the shift in the scale of the study from a continuum to a micro-meso scale in contemporary research [13]. Notably, there has been a surge in adopting a coupled modeling approach to address different facets associated with the HE problem, reflecting a growing recognition of the multidisciplinary nature of the problem. Many theoretical and numerical studies have emerged over the last few decades investigating different aspects, from H uptake to the deformation and fracture characteristics of metals and alloys in contact with different environmental sources. Most of these studies have emphasized accurately resolving the H diffusion phenomenon, which encompasses uptake, transport, and distribution that involves complex H interactions with various microstructural defects. The first part of the review begins with a brief of common HE mechanisms followed by a comprehensive discussion of the various developments made in H diffusion modeling, ranging from fundamental Fickian equations to complex models, covering different aspects such as H transport by mobile dislocations and influence of boundary conditions, crack tip mechanics, and material microstructure. Central to these developments is the pivotal role of the finite element method (FEM), which has emerged as a versatile numerical tool to solve coupled sets of governing equations related to elastoplastic deformation, fracture, and H diffusion.

In the second part, the attention shifts to various computational modeling developments aimed at simulating the role of H in influencing mechanical properties and fracture characteristics of different metals and alloys, notably subcritical cracking and H-assisted crack growth rates. These developments encompass a spectrum of theoretical models, continuum-based finite element simulations, and micro-meso scale investigations alongside applications of fracture models. Notably, the review highlights recent breakthroughs in H-assisted crack growth modeling using state-of-the-art fracture models, emphasizing an increasing adoption of coupled deformation-diffusion-fracture methodologies. In particular, phase field (PF) models represent a recent class of fracture modeling approaches with promising capabilities, including implicit tracking of complex crack surfaces and the absence of geometric restrictions on crack shape and size. These attributes render PF models suitable for multiphysics problems, especially HE problems. At the micro-meso scale, computational physics-based frameworks such as discrete dislocation dynamics (DDD) and crystal plasticity (CP) simulations are gaining traction for studying HE mechanisms at a larger scale.

This comprehensive review provides an in-depth review of the advances in the coupled analysis of H diffusion, deformation, and fracture to study different HE aspects using theoretical and numerical modeling methodologies. The review is structured as follows: Section 2 provides a brief overview of some of the commonly adopted mechanisms or models in the literature to explain HE. Section 3 is dedicated to various developments in H diffusion modeling. Section 4 explores the multiple developments in computational modeling of H-assisted deformation and fracture. Section 5 highlight some challenges and future perspectives. Finally, conclusions are summarized in Section 6.

## 2. Hydrogen embrittlement mechanisms

HE is traditionally defined as the degradation of the ductility and load-carrying capacity caused by H atoms in the lattice structure of metals and alloys [23]. However, depending on various factors, the role of H in this degradation can be further classified as reversible or irreversible. HE is generally referred to as reversible in literature, which involves the accumulation of H atoms at potential cracking sites without any H gas precipitation and typically requires an applied force [24]. Researchers investigating the interaction between H and metals/alloys have proposed numerous mechanisms to explain HE, such as the HEDE, HELP, HESIV, AIDE, and NVC. However, consensus on a single mechanism to explain HE phenomena has not been reached.

### 2.1. *H*-enhanced decohesion

HEDE is one of the first recognized mechanisms to explain HE and has been widely used in numerous numerical studies. It was initially proposed by Pfeil et al. [27] in 1926 following observations of brittle fracture surfaces in H-charged single-crystal and polycrystalline iron. According to HEDE, segregating H atoms at interfaces weakens the cohesive metallic interatomic interactions (bond strength), leading to ruptures at lower stress levels. Notably, a sufficiently high concentration of H must be present within the fracture process zone (FPZ) near the crack-tip, such that the tensile stress exceeds cohesive strength. An important aspect of HEDE is the role of mobile H atoms. Mobile H refers to H atoms that can move through the crystal lattice and along defects. This mobility allows H to accumulate in regions of high stress and near crack tips, enhancing the localized weakening of bonds due to interactions between mobile H and deformation. The potential regions of HEDE encompass the dislocation shielding region, sites with high hydrostatic stresses, and trapping sites such as grain boundaries and interfaces between particles and the matrix. A dislocation shielding region refers to a localized area around a dislocation in a crystal lattice where the mobility of H atoms is reduced or inhibited. Fig. 1a shows a schematic of HEDE involving the weakening of interatomic bonds by (i) lattice H, (ii) adsorbed H, and (iii) H at particle-matrix interfaces. The HEDE model finds support from observations of intergranular fracture as well as theoretical calculations using quantum mechanics and molecular simulations [28–32].

### 2.2. *H*-enhanced local plasticity

The HELP mechanism, initially proposed by Beachem in 1971 [33] and further enhanced by Birnbaum and colleagues [34–36], explains how H promotes localized deformation processes such as accelerated plasticity when H is present at sufficient concentration leading to fracture which is macroscopically brittle in behavior. Fig. 1b depicts the HELP mechanism with a highly localized plasticity zone in the crack-tip region, where high H concentration increases the nucleation and movement of dislocations. The interactions between the H atmosphere and dislocations have received special attention in research on the HELP mechanism, offering valuable insights. Like Cottrell's carbon atmosphere, the H atmosphere forms when H binds to dislocation cores and is drawn to the elastic field around them [34,37]. Within specific conditions, the H atmosphere accelerates the motion of dislocations, and researchers have directly observed this phenomenon in experiments [35,38,39]. In the case of edge dislocations, the H atmosphere creates a shielding effect by altering the stress field of dislocations that reduces the interaction energy between dislocations and then promotes increased dislocation mobility [34,37,39].

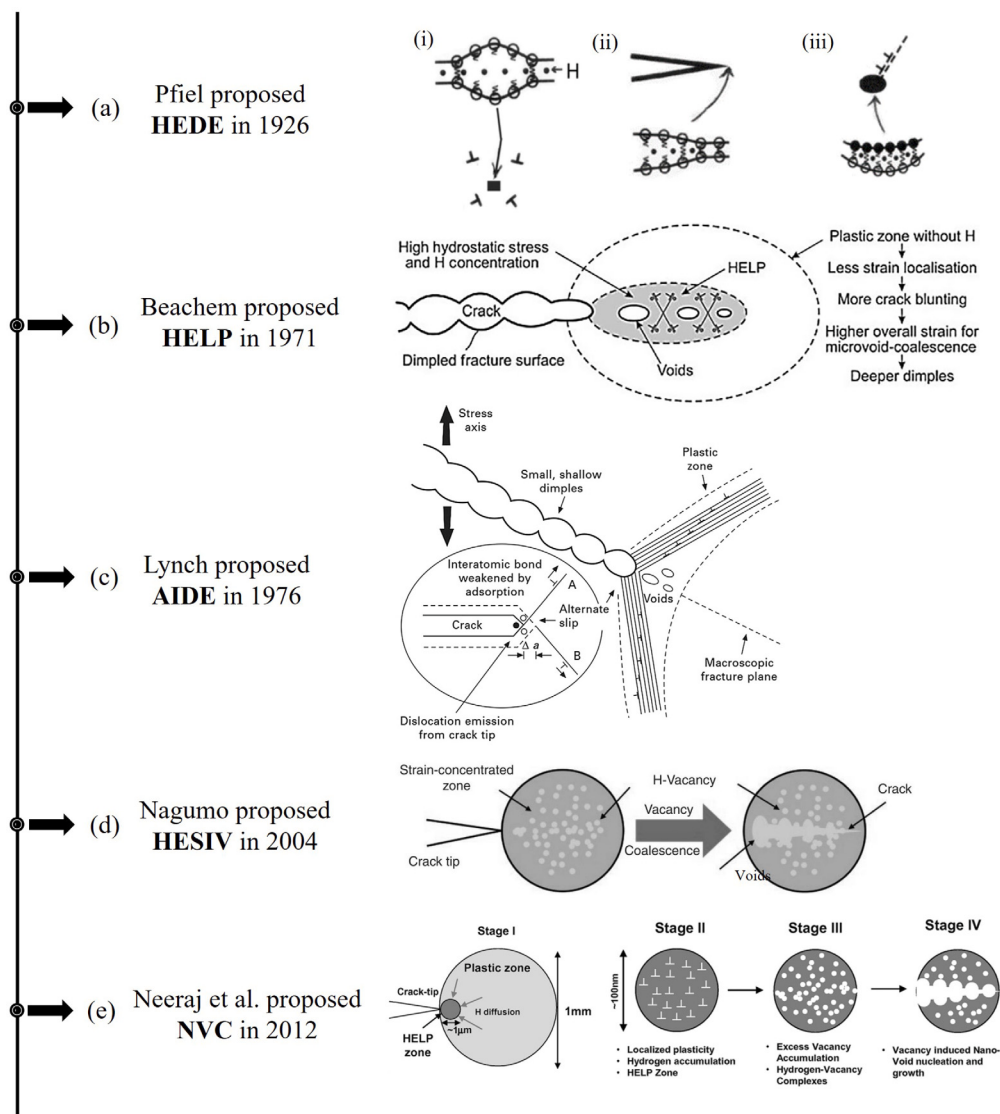


**Fig. 1.** Historical overview and schematic description of some commonly used mechanisms to explain HE [25,26].

### 2.3. Adsorption induced dislocation emission

The AIDE mechanism, developed by Lynch et al. [40,41], suggests that absorbed H atoms on the crack surface decrease the energy barrier for dislocation core formation and surface step motion by breaking and recreating interatomic bonds over multiple atomic distances, which promotes dislocation emission. Fig. 1c provides a visual illustration of AIDE, which also encompasses the nucleation and growth of microvoids. However, dislocation emission remains the primary driver of crack growth. Dislocation emission is a fundamental process in the plastic deformation and fracture of metals, involving dislocation nucleation, movement, and interaction away from the crack-tip. In contrast, the HELP mechanism suggests improved dislocation mobility as the main reason for crack growth. Moreover, the AIDE model emphasizes the role of externally absorbed H, rather than internal H within the bulk material, in significantly enhancing dislocation emission. Various atomistic studies and surface-science observations support the AIDE mechanism [42–45].

### 2.4. H-enhanced strain-induced vacancies

The HESIV mechanism proposes a synergistic effect between H in metals/alloys and strain-induced vacancy generation, where the

presence of H promotes the dislocation motion-induced plasticity and reduction in vacancy formation energy, which facilitates an increase in the density and clustering of vacancies within a material [46–48]. These vacancies can merge to form microvoids, which combine to create larger voids, ultimately reducing crack propagation resistance and leading to premature failures [47]. Fig. 1d presents a schematic illustration of the HESIV mechanism [26]. Supporting evidence for the HESIV mechanism has been obtained from thermal desorption spectrometry (TDS) data, which revealed an increased density of strain-induced vacancies in iron and low-alloyed ferritic steels [46,47]. Further confirmation of the HESIV mechanism comes from positron lifetime measurements. These measurements showed that the mean positron lifetime in iron increased under tensile straining conditions, and this increase was even more pronounced in the case of pre-charged H [49].

### 2.5. Combination of mechanisms

While mechanisms such as HEDE, HELP, AIDE, and HESIV have proven effective under specific conditions, a consensus is emerging among researchers that multiple mechanisms may coexist to explain HE [13,18,19]. For example, the HELP mechanism assumes control when H-assisted fractures are initiated at slip band intersections, whereas the HEDE mechanism operates during decohesion at any

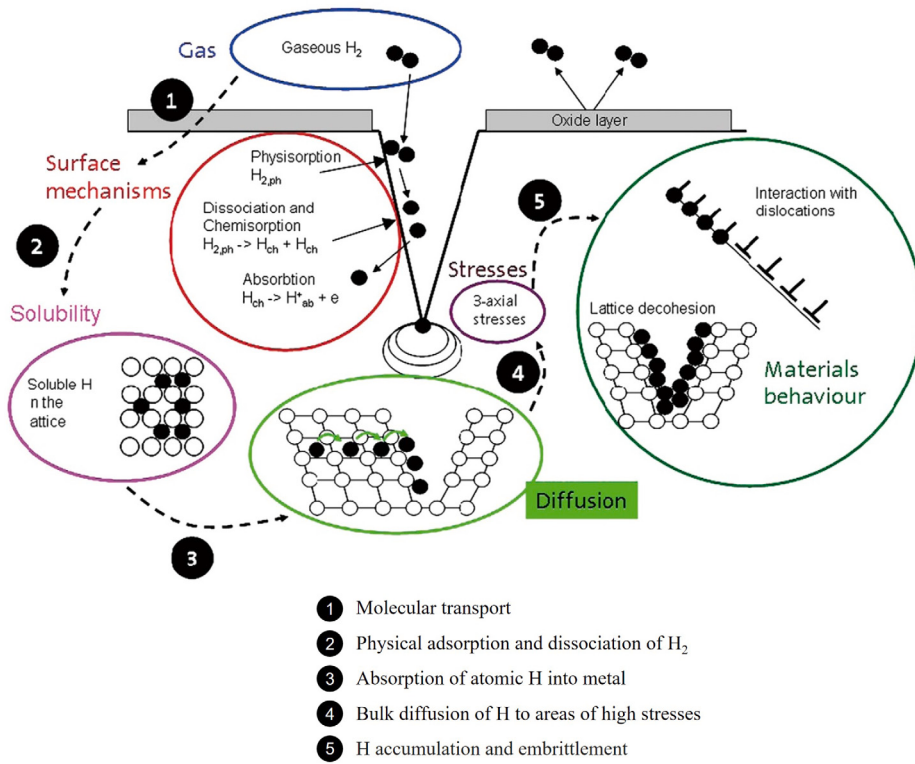


Fig. 2. A schematic illustration of the development of H atoms and its interaction with material [52,53].

interface. An insightful interpretation involves a combination of mechanisms, as seen in the HEDE + HELP model and their synergistic interplay [13,20,21]. Wang et al. [50] and Martin et al. [51] observed brittle intergranular fracture surface characteristics and evolved deformation microstructure beneath intergranular fracture, in support of the combined effect of the HEDE and HELP mechanisms. Recently, Djukic et al. [13] provided a detailed review of the combined interplay of various HE mechanisms in steels, focusing on a combination of the HEDE and HELP models to explain HE. Other than a combination of HELP and HEDE, various synergistic interplays between HE mechanisms can occur under certain conditions depending on the material [12]. Recently, a nanovoid coalescence (NVC) mechanism was developed by Neeraj et al. [22] that aims to provide a complete mechanistic explanation for HE in ferritic steels while taking material microstructure into account. This mechanism, encompassing HEDE, HELP, and HESIV effects, envisions stages leading to fracture with reduced toughness, as depicted in Fig. 1e. Initially, deformation and dislocation plasticity occur in regions of high H concentration (HELP zone). Subsequently, excess vacancies accumulate and stabilize through H bonding, culminating in nanovoid nucleation and growth, ultimately resulting in fracture. Refer to Lynch [25] and Barrera et al. [12] for a more detailed review of various HE mechanisms.

### 3. Hydrogen diffusion modeling

HE is a multifaceted process that starts with the ingress or uptake of H atoms into metals and alloys through exposure to various sources, leading to a decline in their mechanical properties. The H uptake in itself is a detailed process that can be further divided into different stages, starting with the physical adsorption of the source on a solid material surface, followed by a chemical absorption stage, where surface-related processes influence the intake of atomic H from the surrounding environment and involve mechanisms such as adsorption-absorption [53]. The final stage is bulk H transport, which entails

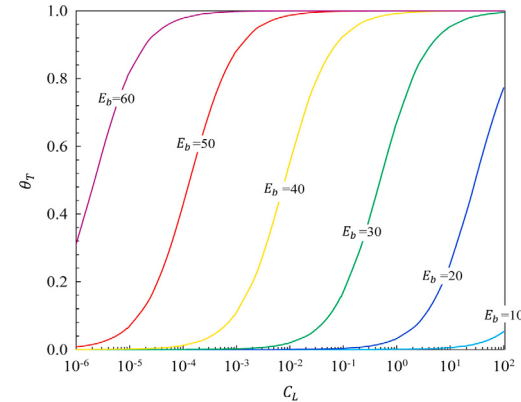


Fig. 3. Relationship between the trapped H occupancy  $\theta_T$  and lattice H concentration  $C_L$ , for different values of trap binding energy  $E_b$  ( $\text{kJ mol}^{-1}$ ) [54].

the diffusion of monoatomic H through the crystal lattice or along grain boundaries inside the material and its aggregation under the effects of localized stresses and material microstructure. For instance, Fig. 2 shows a detailed schematic illustrating a chain reaction of H atom evolution and its interactions for the case of gaseous charging in steel [52,53]. Accurate modeling of these stages by coupling H diffusion, deformation, and fracture is imperative for understanding the complexities of HE. Most coupled modeling studies primarily focus on the bulk H transport stage, which entails H transport through crystal lattices and distribution under the influence of various microstructural trap sites and stress-strain inhomogeneity due to material microstructure. This section presents detailed insights into these developments, from early works to the most recent developments.

### 3.1. Influence of trap binding energy

Various factors influence H distribution inside a material, with trapping sites playing a significant role due to their more favorable energetic conditions for retaining H atoms that restrict H mobility within the material. The seminal work of Sofronis and McMeeking [55] is regarded as the most important early attempt to capture the influence of trapping and hydrostatic stresses on H distribution inside the material, where H diffusion is coupled to elastoplastic deformation based on J2 plasticity theory while explicitly considering H trapping at material defects based on Oriani's theory of "local equilibrium". In their work, Sofronis and McMeeking [55] investigated a blunting crack-tip problem to study the effect of the hydrostatic stress field on H diffusion near plastically deformed regions. The theoretical framework for H transport in Sofronis and McMeeking [55] is particularly widely adopted, and Sofronis and his co-workers [55–57] along with various other researchers have made further contributions to it. Based on these works, notably Sofronis and McMeeking [55], the total H concentration  $C$  can be divided into a lattice H concentration  $C_L$  in normal interstitial lattice sites (NILS) and trapped H concentration  $C_T$ , where  $C_L$  at NILS is expressed as,

$$C_L = \beta_L \theta_L N_L \quad (1)$$

where  $\beta_L$  represents the number of NILS per solvent atom,  $\theta_L$  is the occupancy or fractional coverage of H at NILS ( $0 \leq \theta_L \leq 1$ ), and  $N_L$  is the density of host metal lattice measured as the number of solvent atoms per unit lattice volume, such that  $N_L = N_A / \bar{V}_H$ , where  $N_A = 6.0232 \times 10^{23}$  is the Avogadro number, and  $\bar{V}_H$  is the partial molar volume of H in solid solution. The  $\beta_L$  is typically considered equal to 6 in the case of bcc lattices and 1 in the case of fcc lattices [58,59]. Similar to Eq. (1), the trapped H concentration  $C_x^{(i)}$  for a particular  $i$ th type of trap site can be expressed as [55],

$$C_x^{(i)} = \alpha_T^{(i)} \theta_T^{(i)} N_T^{(i)} \quad (2)$$

where  $\alpha_T^{(i)}$  represents the number of H atom sites per  $i$ th trap type,  $\theta_T^{(i)}$  is the occupancy or fractional surface coverage of H at  $i$ th trap site, and  $N_T^{(i)}$  is the H trapping density for a given  $i$ th trap. As a solute atom, H exists in two states, where  $C_L$  refers to diffusible H that can migrate between lattice sites, and  $C_T$  localizes around microstructural defects, which act as H trap sites. Considering the role of multiple trap sites, the total H concentration  $C$  can be expressed as the sum of H concentration at the lattice sites and each trap site,

$$C = C_L + C_T = C_L + \sum_i^{n_x} C_x^{(i)} \quad (3)$$

where  $n_x$  denotes the total number of trap types. Note that the subscript  $L$  refers to lattice sites, and the subscript  $T$  refers to trap sites. The mass conservation requirement for the total H concentration (lattice and trapped) in a given arbitrary volume,  $\Omega$  with surface  $S$ , is given as [55],

$$\frac{\partial}{\partial t} \int_{\Omega} C d\Omega + \int_S \mathbf{J}_L \cdot \mathbf{n} dS = 0 \quad (4)$$

where  $\mathbf{J}_L$  is the lattice H diffusion flux through the surface  $S$  with the outward-pointing unit normal  $\mathbf{n}$  to the surface  $S$ . The mass conservation requirement implies that the rate of change of H concentration in an arbitrary volume  $\Omega$  must equal the flux through the surface  $S$  bounding the volume. After applying the divergence theorem, the strong form of the local mass balance for H transport following Fick's second law of diffusion can be defined as [55],

$$\frac{\partial C}{\partial t} + \nabla \cdot \mathbf{J}_L = 0 \quad (5)$$

where  $\nabla$  is the gradient operator,  $(\cdot)$  denotes divergence, and  $\mathbf{J}_L$  is expressed via a linear Onsager relationship as follows [55],

$$\mathbf{J}_L = -\frac{DC_L}{RT} \nabla \mu_L \quad (6)$$

where  $D$  is an ideal lattice H diffusivity,  $R$  is the gas constant,  $T$  is an absolute temperature, and  $\mu_L$  is the chemical potential [55],

$$\mu_L = \mu_L^0 + RT \ln \frac{C_L}{N_L} - \bar{V}_H \sigma_H \quad (7)$$

The symbol  $\mu_L^0$  represents the reference chemical potential, and  $\sigma_H$  refers to hydrostatic (mean) stress  $\sigma_H = (\sigma_{11} + \sigma_{22} + \sigma_{33})/3$ . This modified form of Fick's diffusion is usually adopted in most coupled deformation-diffusion models, where both concentration and hydrostatic stress gradient govern H diffusion. After substitution, the H diffusion flux  $\mathbf{J}_L$  in a simplified form reads,

$$\mathbf{J}_L = -D \nabla C_L + \frac{DC_L}{RT} \bar{V}_H \nabla \sigma_H \quad (8)$$

Again substituting Eq. (8) in Eq. (5), the transient H diffusion equation takes the following form [55],

$$\left( \frac{\partial C_T}{\partial t} + \frac{\partial C_L}{\partial t} \right) - \nabla \cdot (D \nabla C_L) + \nabla \cdot \left( \frac{DC_L \bar{V}_H}{RT} \nabla \sigma_H \right) = 0 \quad (9)$$

In Sofronis and McMeeking [55], an effective diffusion coefficient is proposed to describe delayed diffusion due to H trapping, building upon the work by McNabb and Foster [74] and Oriani [75]. McNabb and Foster [74] introduced the kinetics of trapping and de-trapping to Fick's second law of diffusion to model the capture and release of H from traps. The variation of trapped H concentration at a particular trap site can be defined as [76–78],

$$\frac{\partial C_x^{(i)}}{\partial t} = N_T^{(i)} \left[ k_r C_L \left( 1 - \theta_T^{(i)} \right) - p_r \theta_T^{(i)} \right] \quad (10)$$

where  $k_r$  and  $p_r$  are the forward and reverse reaction rate constants related to trapping and detrapping to lattice sites. A low lattice H occupancy ( $\theta_L \ll 1$ ) is assumed for Eq. (10), which is a common assumption for iron-based alloys, particularly in the context of plastic deformation [77–79]. This assumption arises because H has low solubility in iron-based alloys due to various factors [12,80]. Moreover, during plastic deformation, various defects are introduced into the metal and alloys, which act as preferential trapping sites for H atoms and effectively reduce the H occupancy at NILS. Further, McNabb and Foster [74] assumed a constant  $N_T^{(i)}$  which modifies the LHS of Eq. (10) as [77,78],

$$\frac{\partial C_x^{(i)}}{\partial t} = N_T^{(i)} \frac{\partial \theta_T^{(i)}}{\partial t} \quad (11)$$

After substituting Eq. (11), Eq. (10) takes the following form,

$$\frac{\partial \theta_T^{(i)}}{\partial t} = k_r C_L \left( 1 - \theta_T^{(i)} \right) - p_r \theta_T^{(i)} \quad (12)$$

Note that  $k_r$  and  $p_r$  take different units, and Eq. (12) can also be expressed in terms of  $\theta_L$  rather than  $C_L$  [77–79,81],

$$\frac{\partial \theta_T^{(i)}}{\partial t} = k_r^* \theta_L \left( 1 - \theta_T^{(i)} \right) - p_r \theta_T^{(i)} \quad (13)$$

where  $k_r^* = k_r N_L$ . Oriani [75] extended their work to introduce the concept of local chemical equilibrium between the concentration of H in trap sites and mobile H in NILS, and provides a steady-state solution of Eq. (13) ( $\partial \theta_T^{(i)} / \partial t = 0$ ), expressed as [55,75,79],

$$\frac{\theta_T^{(i)}}{1 - \theta_T^{(i)}} = K_T^{(i)} \theta_L \Rightarrow \theta_T^{(i)} = \frac{K_T^{(i)} \theta_L}{1 + K_T^{(i)} \theta_L} \quad (14)$$

where  $K_T^{(i)} = k_r^* / p_r$  is the trap equilibrium constant, which relates to the binding energy  $E_b^{(i)}$  for a specific  $i$ th microstructural trap as [55],

$$K_T^{(i)} = \exp \left( \frac{-E_b^{(i)}}{RT} \right) \quad (15)$$

**Fig. 3** shows the relationship between  $\theta_T$  and  $C_L$  for different trap binding energy values, following Oriani equilibrium theory [75]. Krom

**Table 1**  
Trap binding energies for some H traps in iron and steels [60].

Trap site	Binding energy $E_b$ [kJ/mol]	Material	Ref.
Dislocation	24–26.8	Ferritic	[61,62]
	10–20	Austenitic	[63–65]
Screw dislocation core	20–30	–	[58]
Grain boundaries	17.2–59	–	[58,61,62,65,66]
Lath boundaries	17.8–18.6	–	[67]
Cementite particles	10.9	–	[68]
Martensite/Austenite interface	22	–	[67,69]
Microvoids	35.2–40	–	[61,69]
Austenite/dislocation boundary	37	–	[69,70]
Vacancies	38.6–77.2	–	[46,71–73]

**Table 2**  
Relationship between trapping density function  $N_T$  and equivalent plastic strain  $\epsilon_p$ .

Material	Relation	Ref.
$\alpha$ -Fe	$\log N_T = 23.26 - 2.33\exp(-5.5\epsilon_p)$	Kumnick and Johnson [83]
AISI 1020	$\log N_T = 27.15 - 2.33\exp(-5.5\epsilon_p)$	Huang and Shaw [84]
AISI 4140	$\log N_T = 27.23 - 24.68\epsilon_p^{0.7}$	Colombo et al. [85]
PSB1080 (peened)	$\log N_T = 34.66 - 2.33\exp(-5.5\epsilon_p)$	Wang et al. [86]

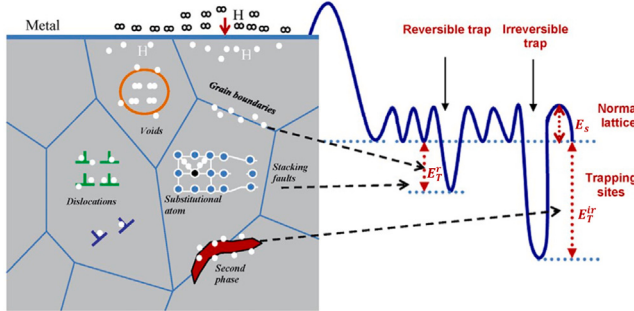


Fig. 4. Common H trap sites (irreversible and reversible types) [87].

and Bakker [79] showed that the assumption in Oriani [75] can be valid for strain rates less than  $\approx 1 \text{ s}^{-1}$ , and Bombac [82] validated it by using Monte Carlo (MC) simulations in defective microstructures. Using Eq. (1), Eq. (2) and (14),  $C_x^{(i)}$  can also be related to  $C_L$  as [55],

$$C_x^{(i)} = C_L \left( \frac{K_T^{(i)} \alpha_T^{(i)} N_T^{(i)}}{\beta_L N_L + K_T^{(i)} C_L} \right) \quad (16)$$

In Eq. (15),  $E_b^{(i)}$  quantifies the energy required for the H atom to escape a particular  $i$ th trap site to move into the host metal lattice, and it varies depending on the type of trap such as dislocations, grain boundaries, and interfaces, each holding H with varying degrees of affinity dictated by their binding energy [62,88]. Fig. 4 illustrate some common H traps (reversible or irreversible) based on a trap strength model by Lee and Lee [89], where  $E_b^r$  and  $E_b^{ir}$  refers to trap binding energy associated with reversible and irreversible traps [87]. Reversible traps (e.g., grain boundaries) have a lower affinity for binding or retaining H atoms than irreversible traps (e.g., second-phase particles), making it easier for H atoms to escape before local H saturation. Table 1 lists the trap binding energies for some common H trap sites in steel [60]. Assuming thermodynamic equilibrium based on the Oriani theory, an effective diffusion coefficient  $D_{\text{eff}}$  can be expressed as function of lattice H diffusivity  $D$  [55,65],

$$D_{\text{eff}} = \frac{D}{1 + \sum_i^{n_x} \frac{\partial C_x^{(i)}}{\partial C_L}} \quad (17)$$

and the modified form of H diffusion given in Eq. (9) reads [55],

$$\frac{D}{D_{\text{eff}}} \frac{\partial C_L}{\partial t} - \nabla \cdot (D \nabla C_L) + \nabla \cdot \left( \frac{DC_L \bar{V}_H}{RT} \nabla \sigma_H \right) = 0 \quad (18)$$

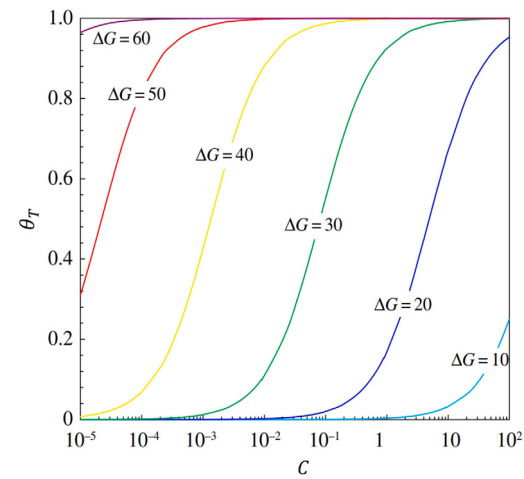


Fig. 5. Relationship between the trapped H occupancy  $\theta_T$  and total H concentration  $C$ , for a range of Gibbs free energy difference  $\Delta G$  (kJ mol<sup>-1</sup>), following the Langmuir–McLean isotherm relation [54].

Based on the H diffusion expression in Eq. (18), the numerical results in Sofronis and McMeeking [55] revealed that the trapped H is the main cause of the locally high H concentration near the crack-tip. As an alternative,  $\theta_T$  can be calculated using the Langmuir–McLean isotherm relation [90], without explicitly considering H trapping in the mass balance [91,92]. The  $\theta_T$  at a decohering interface (e.g., grain boundaries) can be calculated from the bulk H concentration  $C$  as [90, 93, 94],

$$\theta_T = \frac{C}{C + \exp(-\frac{\Delta G}{RT})} \quad (19)$$

where  $\Delta G$  is the Gibbs free energy difference between the interface and the surrounding material. The  $\Delta G$  can be identified by the broad spectrum of experimental data of trap binding energy  $E_b$  for a given trap. The equilibrium construction in Eq. (19) is derived from the McLean model [93], and bears a resemblance to the Langmuir Adsorption Isotherm used for gas adsorption on a free surface [90,94]. Fig. 5 illustrates the relationship between  $\theta_T$  and the bulk H concentration  $C$  for a range of  $\Delta G$ , as predicted by the Langmuir–McLean isotherm relation [90].

### 3.2. Influence of trap density

Typically, the trap density is generally assumed to be constant for traps such as carbide and grain-boundaries [65]. However, experimental studies and many micro-meso scale investigations suggest that microstructure beneath surfaces of specimens fractured in the presence of high concentrations of H indicate that the dislocation structure plays an essential role in establishing the local conditions that promote failure [3,50,95,96]. In many numerical studies, trap density  $N_T$  associated with dislocations is assumed to evolve with plastic straining, and

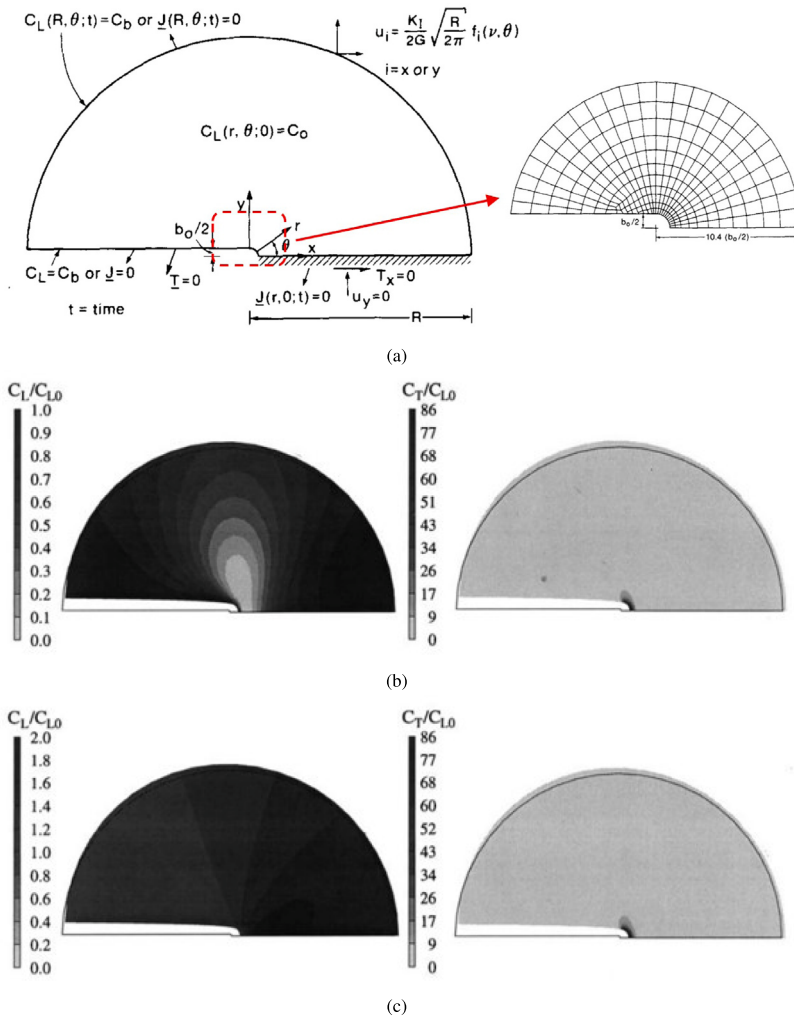


**Fig. 6.** (a) Geometry, initial conditions, and FE mesh for the coupled H diffusion and elastoplastic deformation problem at the blunting crack-tip. A relatively fine mesh is adopted near the crack-tip, as illustrated here. (b) Normalized H distribution at lattice sites  $C_L/C_{L0}$  (left) and trap sites  $C_T/C_{T0}$  (right) for the total loading time of  $t = 1.3 \text{ s}$  and (c)  $t = 1.3 \times 10^6 \text{ s}$  [56]. A region similar to a plastic zone develops at a high strain rate (i.e., total loading time of  $t = 1.3 \text{ s}$ ) with a low lattice H concentration compared to loading at a low strain rate (i.e., total loading time of  $t = 1.3 \times 10^6 \text{ s}$ ).

this relation is experimentally determined [65,83,85,97,98]. Sofronis and McMeeking [55] related  $N_T$  to the equivalent or effective plastic strain  $\epsilon_p$ , based on the experiments in Kumnick et al. [83],

$$\log N_T = 23.26 - 2.33 \exp(-5.5\epsilon_p) \quad (20)$$

Experimental studies by Kumnick et al. [83] showed an increase of as much as 2 orders of magnitude in the  $N_T$  caused by the plastic deformation. Table 2 summarizes equations illustrating some relationships between  $N_T$  and  $\epsilon_p$ , adopted in the literature. Recently, Huang and Guo [99] introduced a new definition for  $N_T$ , where they used a plastic factor  $\tilde{\epsilon}_p$  instead of  $\epsilon_p$ , where  $\tilde{\epsilon}_p$  is a function of damage and  $\epsilon_p$  at a particular time interval.

Krom et al. [56] further modified the H transport model in Sofronis and McMeeking [55],

$$\frac{\partial C_T}{\partial t} = \frac{\partial C_T}{\partial C_L} \frac{\partial C_L}{\partial t} + \sum_i^n \frac{\partial C_x^{(i)}}{\partial N_T^{(i)}} \frac{\partial N_T^{(i)}}{\partial \epsilon_p} \frac{\partial \epsilon_p}{\partial t} \quad (21)$$

where  $\partial \epsilon_p / \partial t$  is a (plastic) strain-rate factor that balances the total H concentration. Substituting Eq. (21) in Eq. (9), the H-balance takes the following form,

$$\frac{D}{D_{\text{eff}}} \frac{\partial C_L}{\partial t} + \sum_i^n \alpha_T^{(i)} \theta_T^{(i)} \frac{\partial N_T^{(i)}}{\partial \epsilon_p} \frac{\partial \epsilon_p}{\partial t} - \nabla \cdot (D \nabla C_L) + \nabla \cdot \left( \frac{DC_L \bar{V}_H}{RT} \nabla \sigma_H \right) = 0 \quad (22)$$

The contour plots of the normalized H distribution are shown in Fig. 6 to graphically represent the effect of the strain-rate factor on H concentrations. Note that the effect of strain rate is investigated in Krom et al. [56] by changing the total loading time to reach a load  $K_I = 89.2 \text{ MPa}\sqrt{\text{m}}$ . At high strain rates (i.e., total loading time  $t = 1.3 \text{ s}$ ), a separate region characterized by very low H concentration within NILS sites and patterned like the plastic zone can be observed in Fig. 6(b). On the other hand, a region that reflects the hydrostatic stress distribution appears at low strain rates (i.e., total loading time  $t = 1.3 \times 10^6 \text{ s}$ ) in Fig. 6(c), except in the vicinity of the blunting crack-tip surface. Notably, independent of the type of boundary condition or strain rate, the region of high H concentration at trap sites stays relatively limited.

In an attempt to study the role of H trapping in steel, Krom and Bakker [79] adopted a micromechanics-based approach where H trap density  $N_T$  is related to the density of dislocations in the deforming material following the work of Lufrano et al. [100]. Assuming one trap site per atomic plane intersected by a dislocation [101,102],  $N_T$  is expressed as,

$$N_T = \lambda \frac{\rho}{a_L} \quad (23)$$

where  $a_L$  is a lattice constant,  $\rho$  is the dislocation density (considering both mobile and immobile dislocations), and  $\lambda$  takes a value of  $\sqrt{2}$  for bcc lattices. Lufrano et al. [100] maintain that the assumption in

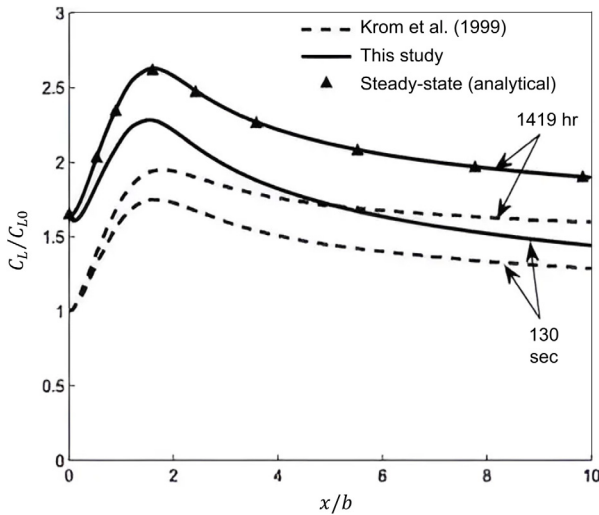


**Fig. 7.** Normalized concentration of H ( $C_L/C_{L0}$ ) in front of the crack-tip ( $x/b$ ) at different time intervals, compared with Krom et al. [56] and analytical solution under isothermal and steady-state conditions [103].

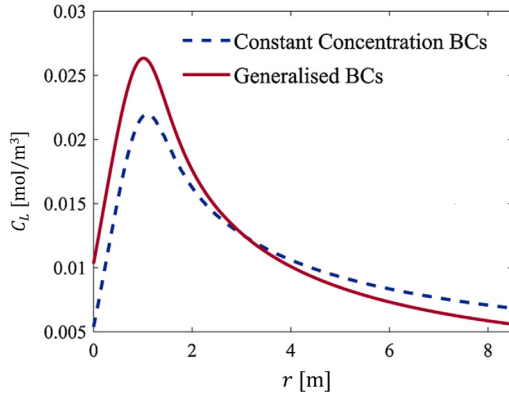


**Fig. 8.** Lattice H concentration  $C_L$  ahead of the crack-tip ( $r$ ) using constant concentration and generalized boundary conditions [77].

Eq. (23) is consistent with the experimental work of Thomas [63] in which the best fit to the experimental data was obtained with a trapping radius of only 1 to 2 atomic spacings. In Sofronis et al. [98], the  $N_T$  is defined as,

$$N_T = \sqrt{2} \frac{\rho}{a_L} \quad (24)$$

where  $\rho$  is the dislocation density (dislocation line length/m<sup>3</sup>), that varies linearly with logarithmic strain  $\epsilon$ ,

$$\rho = \begin{cases} \rho_0 + \gamma_d \epsilon & \text{if } \epsilon \leq 0.5 \\ 10^{16} & \text{if } \epsilon \geq 0.5 \end{cases} \quad (25)$$

where  $\rho_0 = 10^{10}$  line length/m<sup>3</sup> denotes the dislocation density for the annealed material and  $\gamma_d = 2 \times 10^{16}$  line length/m<sup>3</sup>. A similar approach was also adopted in Taha and Sofronis [57], assuming  $\lambda = \sqrt{2}$  in Eq. (23) for the evolution of trap density, where finite element simulations were conducted to study H distribution in front of the blunting crack tip under small scale yielding conditions. Their study demonstrates that H trapping leads to a decrease in diffusivity while increasing H solubility.

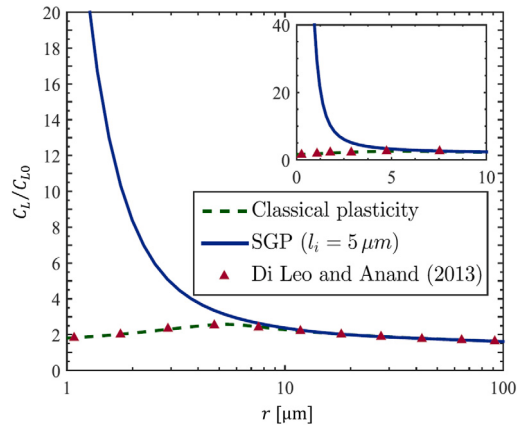


**Fig. 9.** Normalized lattice H concentration ( $C_L/C_{L0}$ ) ahead of the crack-tip ( $r$ ) for SGP and conventional plasticity theory [107].

### 3.3. Influence of boundary conditions

Note that a specific constant H concentration is applied at the crack surface in Sofronis and McMeeking [55] and Krom et al. [56]. An appropriate selection of H concentration on the material boundaries is crucial to reflect the correct H ingress or uptake in the material from the surrounding environment. Typically, in most numerical studies, a constant H concentration boundary condition (Dirichlet-type) is favored due to its simplicity in numerical implementation [85,92,104–106]. However, some investigations opt for a constant surface chemical potential on the boundary to better capture H uptake, accounting for the stress state as well [103,107–110]. One such development includes the work by Di Leo and Anand [103], where a thermodynamically consistent coupled deformation-diffusion theory captures H diffusion in elastoplastic solids. Their work builds upon the previous work of Anand [111] to incorporate significant effects of H trapping at microstructural trapping sites. Unlike [55,56], Di Leo and Anand [103] use lattice chemical potential as the boundary condition instead of constant H concentration, and not only models H trapping [112], but also considers trapping in non-equilibrium situations. Di Leo and Anand [103] predict a higher H concentration, as shown in Fig. 7, which presents the normalized lattice H distribution ( $C_L/C_{L0}$ ) in front of the crack-tip  $x/b$  at the loading end for different time intervals  $t = 130$  s and  $t = 1419$  h.

As an alternative to Dirichlet-type boundary conditions, recently Martinez-Paneda et al. [77] proposed generalized boundary conditions to study H transport near the crack-tip, where a generalized flux  $J_{in}$  is prescribed at the crack surfaces as follows,

$$J_{in} = k_c (1 - \theta_{ad}) - k_{r,chem} \theta_{ad}^2 - k_{r,elec} \theta_{ad} \quad (26)$$

where  $\theta_{ad}$  fractional surface coverage associated with adsorbed H,  $k_c$  is the charging current constant,  $k_{r,chem}$  is the chemical recombination constant, and  $k_{r,elec}$  is the electrochemical recombination constant. The constants  $k_c$ ,  $k_{r,chem}$ , and  $k_{r,elec}$  are associated with adsorption, chemical recombination, and the electro-chemical recombination processes for an electrochemistry-diffusion interface and can be determined experimentally. Fig. 8 shows the lattice H concentration ahead of the crack-tip for a case study on AISI 4340 steel considering constant H and generalized boundary conditions. The illustrated H distribution corresponds to an applied load  $K_I = 30$  MPa $\sqrt{\text{m}}$  and a total loading time of  $t = 10^5$  s. Notably, a significantly higher crack-tip H concentration is observed using generalized boundary conditions on the crack surface than constant H concentration boundary conditions.

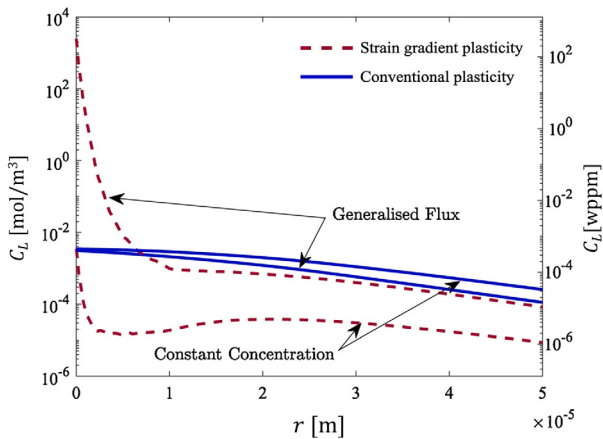


**Fig. 10.** Lattice H concentration  $C_L$  ahead of the crack-tip ( $r$ ) predicted by SGP and conventional plasticity theory [77].

### 3.4. Influence of crack-tip mechanics

Generally, cracking occurs close to the crack-tip, often within microns, where the increased dislocation density due to the large gradients of plastic deformation promotes dislocation-based strain hardening, resulting in higher stress concentrations at the crack-tip. Conventional plasticity theory provides limited insights into this hardening behavior and falls short of capturing the high crack-tip stresses. SGP theory, on the other hand, captures the local strengthening observed when the macroscopic strain field varies over microns by linking statistically stored dislocations (SSDs) and geometrically necessary dislocations (GNDs) to plastic strain and strain gradient. Following dislocation-based hardening theories, the total dislocation density  $\rho$  along any particular slip system  $\alpha$  can be defined as the sum of SSD density  $\rho_{SSD}$  and GND density  $\rho_{GND}$ . SSDs do not accommodate lattice curvature and arise from distributed nucleation, slip, and stochastic pinning events by obstacles, leading to a zero net open Burgers circuit. GNDs arise from plastic strain gradients and accommodate permanent lattice curvature due to non-uniform plastic deformation.

Notably, large gradients of plastic strain are present in front of the crack-tip associated with lattice curvature that promotes local hardening, thereby necessitating to include the role of GNDs in accommodating lattice curvature [3,107,113]. Martinez-Paneda et al. [107] incorporated the role of GNDs towards local hardening through SGP theory and investigated its influence on H diffusion near the crack-tip. They adopt the strain gradient generalization of the J2 flow theory proposed by Fleck and Hutchinson [114] to account for GNDs in the continuum modeling based on a phenomenological strain gradient plasticity (PSGP) approach, where plastic strain gradients are incrementally captured through the generalized plastic strain rate  $\dot{\epsilon}_p$  as a function of conventional effective plastic strain rate  $\dot{\epsilon}_p$  as [113],

$$\dot{\epsilon}_p = \sqrt{\dot{\epsilon}_p^2 + h_1^2 I_1 + h_2^2 I_2 + h_3^2 I_3} \quad (27)$$

where  $\dot{\epsilon}_p = \sqrt{(2/3)\dot{\epsilon}^p : \dot{\epsilon}^p}$ ,  $I_i$  represent three unique non-negative invariants of plastic strain rate tensor  $\dot{\epsilon}^p$ , and  $h_1, h_2, h_3$  are the material parameters that can be obtained from the fit of experimental measurements. Fig. 9 shows the normalized lattice H concentration ahead of the crack-tip using SGP and conventional J2 plasticity theories. Notably, this comparison reveals a significantly high concentration of lattice H at the crack-tip for the case of SGP compared to conventional plasticity, thereby emphasizing the role of GNDs towards the local elevation of crack-tip stresses in the FPZ through SGP.

To highlight the role of dislocation-based hardening, Martinez-Paneda et al. [77] proposed a generalized framework that combines

SGP and generalized flux boundary conditions to investigate H transport near the crack-tip. They adopt a higher order SGP model by Gudmundson [115] that promotes additional storage of dislocations required to accommodate lattice curvature associated with plastic strain gradients, which are captured through the generalized effective plastic strain rate  $\dot{\epsilon}_p$ ,

$$\dot{\epsilon}_p = \left( \frac{2}{3} \dot{\epsilon}_p^2 + L_d^2 \nabla \dot{\epsilon}_p^2 \right)^{0.5} \quad (28)$$

where  $L_d$  is a dissipative material length scale that quantifies the degree to which the material exhibits dissipative strengthening. Fig. 10 shows the lattice H concentration ahead of the crack-tip, highlighting the role of dislocation hardening. The comparison reveals the crucial role of dislocation hardening, as a significant difference is observed between the crack-tip H concentration for SGP and conventional J2 plasticity cases.

### 3.5. Influence of microstructure

Many experimental investigations have revealed that the various microstructural features influence H diffusion [118–121]. In recent years, crystal plasticity finite element (CPFE) simulations have offered a practical and effective approach to capturing plastic deformation in crystalline materials driven by the dislocation movements on the activated slip systems. A CP framework incorporates slip kinematics, slip rules, and grain interactions to derive constitutive equations that capture the collective behavior due to heterogeneous deformation involving individual or clusters of grains with varying orientations. Various recent works have adopted CPFE to comprehensively capture the interplay of material microstructure, external loads, and their influence on H distribution, segregation, and HE mechanisms [116,122–126]. For example, Ilin et al. [122] studied the influence of stress-strain heterogeneities on the H distributions in a synthetic material microstructure using coupled H diffusion-CPFE simulations. They observed H accumulation in the regions with high hydrostatic stresses, typically near the grain boundaries, while finding that trapping had an insignificant effect. Hassan et al. [124] applied coupled H diffusion-CPFE simulations to study the trapping influence of dislocations and plastic prestraining on H distribution in virtual polycrystalline microstructures. The H transport model of Sofronis and McMeeking [55] and Krom et al. [56] is used to capture the influence of trapping and hydrostatic stresses. Within a CP framework, as shown in Hassan et al. [124], plastic deformation is associated with dislocations glide on active slip systems  $\alpha$  solely based on the dislocation slip as the deformation process. The constitutive evolution of slip shear rate  $\dot{\gamma}^\alpha$ , which describes the rate of plastic deformation or dislocations movement at the crystal level, is defined as,

$$\dot{\gamma}^\alpha = \dot{\gamma}_0 \left| \frac{\tau^\alpha - \chi_b^\alpha}{\tau_c^\alpha} \right|^M \text{sign}(\tau^\alpha + \chi_b^\alpha) \quad (29)$$

where  $\tau^\alpha$  is the resolved shear stress in the dominant slip system  $\alpha$  with the slip resistance  $\tau_c^\alpha$ ,  $\dot{\gamma}_0$  is the reference slip shear rate,  $M$  is a power law exponent quantifying the rate sensitivity of slip,  $\tau_c^\alpha$  is the critical resolved shear stress and  $\chi_b^\alpha$  is the resolved back-stress on the glide system to include kinematic hardening effect, postulated by Rice [127] and Hutchinson [128]. The resolved shear stress determines the ease of dislocation movement, such that shearing occurs on the slip system subjected to the largest resolved shear stress  $\tau_c^\alpha$ . The study by Hassan et al. [124] concludes that effective diffusivity decreases with stronger traps. This effect becomes more pronounced at material deformations, leading to a considerable increase in trapped H concentration. However, a direct quantitative comparison with experimental data was not performed. In another study, Hussein et al. [116] investigated the distribution of H atoms in an artificial microstructure with grain-scale anisotropy generated using a representative volume element (RVE) through a coupled H diffusion-CPFE simulations, where they

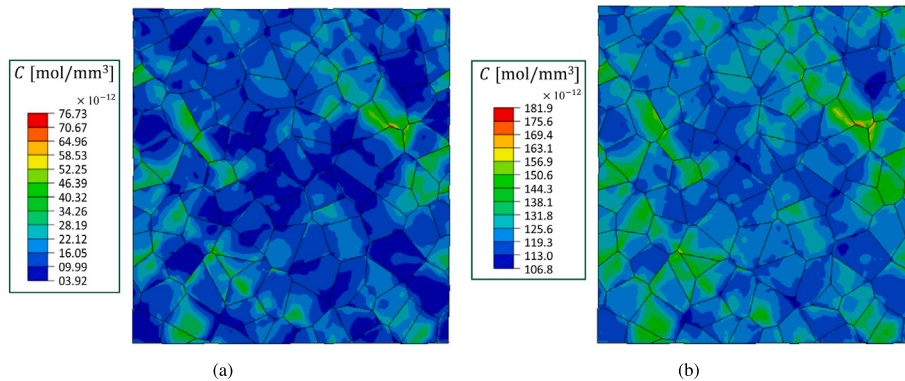


**Fig. 11.** The H distribution in the polycrystal for the gaseous H pressure (a)  $p_{\text{H}_2} = 1$  bar, and (b)  $p_{\text{H}_2} = 1000$  bar [116].

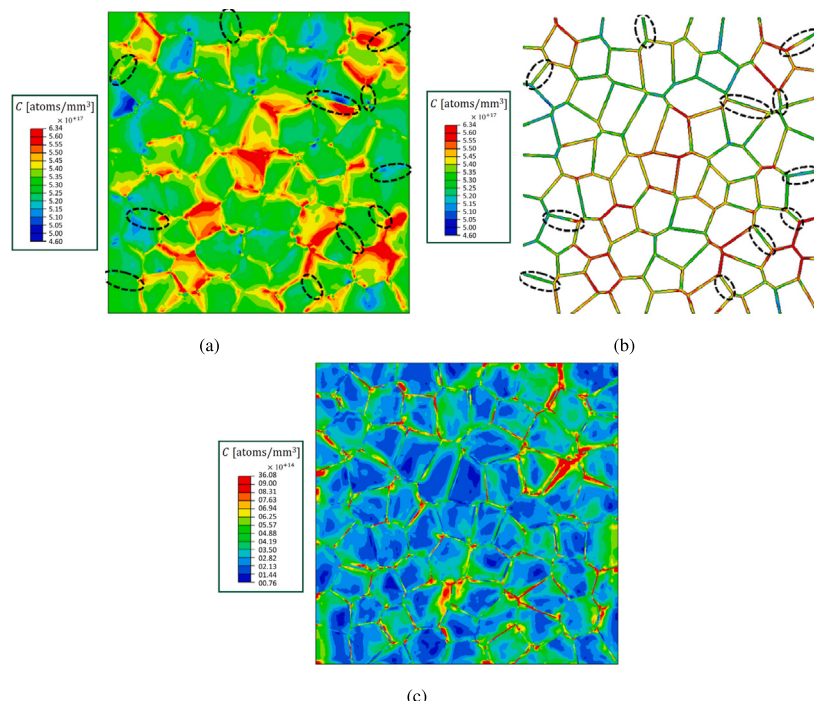


**Fig. 12.** (a) Total H concentration  $C$  in polycrystal, (b) total H concentration  $C$  in grain boundaries, and (c) H concentration in dislocation cores  $C_{D,H}$  [117].

explored the impact of heterogeneous micromechanical stress fields on H redistribution. The constitutive evolution of slip shear rate  $\dot{\gamma}^\alpha$  is modeled using a viscoplastic formulation as [129],

$$\dot{r}^\alpha = \dot{a}_0^\alpha \left( \frac{r^\alpha}{g^\alpha} \right) \left| \frac{r^\alpha}{g^\alpha} \right|^{n_s - 1} \quad (30)$$

where  $\dot{a}_0^\alpha$  is the reference strain on slip system  $\alpha$ ,  $n_s$  is an exponent that characterizes material rate sensitivity, and  $g^\alpha$  is the function describing the current strength that evolves as [130],

$$\dot{g}^\alpha = \sum_\beta E_{\alpha\beta} \dot{\gamma}^\beta \quad (31)$$

where  $E_{\alpha\beta}$  is the hardening modulus matrix that empirically captures the micromechanical interaction among different slip systems. The redistribution of H caused by heterogeneous micromechanical strains that increase with gaseous H pressure is shown in Fig. 11. Consistent with previous findings by Hassan et al. [124] using a similar type of approach, the results indicate a buildup of H primarily at grain boundaries due to the heterogeneous micromechanical stress fields leading to a reduction of H atoms from compressive to tensile regions.

The previous discussion describes CPFE simulations based on local CP models that use phenomenological hardening law (see Eq. (31)).

Alternatively, some numerical investigations have adopted dislocation-density-based CP models to investigate H transport in metallic microstructures [117,131,132]. For example, in Kumar and Mahajan [131], a weakly coupled dislocation-density-based H diffusion/trapping-CPFE model to simulate the influence of mechanical loads on H distribution within the material microstructure. In their one-way coupled approach, they adopt a non-local CP approach to incorporate the effect of the strain gradients in the materials hardening laws by introducing SSDs density  $\rho_{SSD}$  and GNDs density  $\rho_{GND}$  to materials hardening equations. The evolution of  $\rho_{SSD}$  is defined as [133],

$$\dot{\rho}_{SSD}^{\alpha} = \left( c_1 \sqrt{\rho^{\alpha}} - c_2 \rho^{\alpha} \right) |\dot{\gamma}^{\alpha}| \quad (32)$$

where the constants  $c_1$  and  $c_2$  govern the dislocation multiplication and annihilation on the slip system  $\alpha$ , and  $\dot{\gamma}^\alpha$  is the slip-rate. Within a nonlocal framework, the deformation at a given material point is strongly coupled to the state of neighboring grains during the evolution of GNDs, which is captured by computing the plastic strain gradients resulting from heterogeneities inside the microstructure, where the GNDs density tensor  $G$  is calculated as the classical Nye tensor to

translate the strain gradient into GNDs,

$$\mathbf{G} = -(\mathbf{F}^p \times \nabla) \quad (33)$$

where  $\mathbf{F}^p$  represents the plastic part of the deformation gradient tensor. The GNDs density tensor  $\mathbf{G}$  represents the sum of total crystallographic GNDs density along the slip system  $\alpha$ , defined as the closure failure of the Burgers circuit with the net Burgers vector. Regarding the plastic flow, the slip rate on the  $\alpha$  slip system is defined using the classical Orowan-law [134] at a material point,

$$\dot{\gamma}^\alpha = \rho^\alpha b v_0 \left| \frac{\tau^\alpha + \tau_{\text{GND}}^\alpha}{\tau_c^\alpha} \right|^{n_s} \text{sign}(\tau^\alpha + \tau_{\text{GND}}^\alpha) \quad (34)$$

where  $b$  is the magnitude of Burgers vector,  $v_0$  is the reference dislocation velocity,  $n_s$  is strain-rate sensitivity, and  $\tau_{\text{GND}}^\alpha$  is the resolved shear stress due to kinematic hardening from the pileup of GNDs. The SSDs and GNDs contribute to the hardening evolution of slip systems based on the Taylor rule as [135,136],

$$\tau^\alpha = c_3 \mu_s b \sqrt{\sum_{\beta=1}^{n_\beta} \chi_{\alpha\beta} \left( \rho_{\text{SSD}}^\beta + \rho_{\text{GND}}^\beta \right)} \quad (35)$$

where  $c_3$  is a constant,  $\mu_s$  is the elastic shear modulus,  $n_\beta$  is the total number of slip systems, and  $\chi_{\alpha\beta}$  is the strength of the interaction between slip systems. The study by Kumar and Mahajan [131] concludes that grain-size reduction enhances the trapping of H atoms, and the distribution of hydrostatic stress dictates H distribution in the material microstructure.

A novel H diffusion modeling approach coupled to CP that considers the influence of grain boundary character on H diffusion in polycrystalline materials is proposed by Li et al. [117]. Their approach offers numerical capabilities to simulate the effect of trapping, de-trapping, and acceleration of H due to the grain boundary. To accomplish this, their H diffusion model uses distinct diffusion characteristics for the grain boundary from the inside of the grain using a quasi-physics-based approach that assumes different sets of H concentrations and associated flux for different regions in a polycrystal. The local mass balance in Li et al. [117] takes the following form,

$$D_{\text{eff}} \frac{dC_p}{dt} + \theta_{\text{D-H}}^\alpha \frac{dN_{\text{D-H}}^\alpha}{d(\rho_{\text{SSD}}^\alpha + \rho_{\text{GND}}^\alpha)} \frac{d(\rho_{\text{SSD}}^\alpha + \rho_{\text{GND}}^\alpha)}{dt} + \nabla \cdot \mathbf{J}_p = 0 \quad (36)$$

where  $C$  refers to H concentration with  $p$  representing an index for different regions ( $L$  for lattice and GB-H for grain boundary),  $N$  denotes the number of sites per unit volume,  $\theta_{\text{D-H}}^\alpha$  is the H occupancy at dislocation cores (represented by the symbol D-H), and  $D_{\text{eff}}$  is the effective diffusion coefficient,

$$D_{\text{eff}} = \sum_{\alpha=1}^{n_\alpha} \frac{N_{\text{D-H},p}^\alpha K_{\text{D-H},p}^\alpha N_p}{\left[ N_p + C_L \left( K_{\text{D-H},p}^\alpha - 1 \right) \right]^2} + 1 \quad (37)$$

where  $n_\alpha$  refers to the number of slip systems, and  $K_{\text{D-H},p}^\alpha$  is the trap equilibrium constant. Note that  $D_{\text{eff}}$  is defined considering Oriani's equilibrium between the H atoms in dislocation cores ( $C_{\text{D-H}}$ ) and lattice/grain boundary ( $C_L$  and  $C_{\text{GB-H}}$ ). The different microstructural features (e.g., grain boundary orientation) and corresponding diffusion behaviors associated with H concentration in different regions of the polycrystals lead to six distinct diffusion modes, which are explicitly defined in Li et al. [117]. Fig. 12(a) illustrates the H distribution inside the polycrystal, highlighting the strong influence of material microstructure where H accumulates near grain boundaries and triple junctions. Fig. 12(b) illustrates H distribution in the grain boundaries, highlighting the influence of grain boundary misorientation where low-angle grain boundaries (encircled by a black line) tend to have low H concentration. Fig. 12(c) illustrates the H concentration in dislocation cores  $C_{\text{D-H}}$  where most dislocation-trapped H atoms tend to accumulate near grain boundaries.

Multiscale modeling approaches offer another promising avenue to bridge the gap between different spatial scales, enhancing our understanding of H diffusion and providing more accurate predictions and insights into HE influenced by microstructure. In one such attempt, Jothi et al. [137] proposed a multiscale modeling approach to investigate HE in polycrystalline materials by coupling a continuum model with a micro-structural model that resolves the necessary micro-structural phenomena (intragranular and intergranular fracture). The multiscale approach uses a coupled micro-structural and continuum critical dislocation site (CMCD) approach, where a substructural model is used to capture the influence of grains, triple junctions, and micro-structural defects in the continuum domain. The numerical results presented in their work highlighted the pivotal role of detailed local microstructural information, such as critical sites and interfacial areas, on H diffusion and accumulation. In a similar type of work, Jothi et al. [138] studied H transport, segregation, and trapping (based on the McNabb trap model) using multiscale, multiphase simulations on polycrystalline microstructures. Notably, the results also revealed a pronounced inhomogeneity in H concentration, with grain boundaries accumulating significantly higher levels of H than the grains themselves.

### 3.6. Influence of mobile dislocations

Mobile dislocations can also act as potential weak H traps (due to low binding energy [139]), thereby influencing H transport by dragging along absorbed H or contributing to the localized accumulation of H. Various experiments support H diffusion by mobile dislocations [140–142], and recently some numerical studies have investigated this topic by coupling H diffusion and deformation [143–146]. For example, Dadfarnia et al. [143] extended the H-transport model by Sofronis and his colleagues [55,57], incorporating the role of moving dislocations as H traps. In their approach, the velocity vector of dislocations governs the H transport flux, consistently directing it from the crack-tip towards the material's interior. This extension yields a modified form of the local balance in Eq. (5), which can be expressed as,

$$\frac{\partial C}{\partial t} + \nabla \cdot (\mathbf{J}_L + \mathbf{J}_D) = 0 \quad (38)$$

where  $\mathbf{J}_L$  represents the H diffusion flux through NILS and  $\mathbf{J}_D$  stands for the H diffusion flux associated with moving traps,

$$\mathbf{J}_D = N_T^m \mathbf{V}^d (\alpha \theta_T^d) \quad (39)$$

where  $\mathbf{V}^d$  is the dislocation velocity vector, and  $N_T^m$  represents the H trapping density for mobile dislocations with associated H occupancy  $\theta_T^d$ . According to Dadfarnia et al. [143], H increases the formation of mobile and immobile dislocations through accelerated interactions, affecting H trap density. To quantify the H trap density associated with mobile dislocations, Eq. (23) takes the following form,

$$N_T^m = \lambda \frac{\rho_m}{a} \quad (40)$$

where  $\rho_m$  is the mobile dislocation density. Charles et al. [144] extended the modeling framework in Dadfarnia et al. [143] by incorporating trapping and detrapping kinetic equations, H dragging by mobile dislocations, and the H breakaway from fast-moving dislocations.

Taking advantage of CP for a more comprehensive modeling of H diffusion phenomena, Yuan et al. [145] proposed an H transport model that builds upon Dadfarnia et al. [143] considering the role of mobile dislocations and plastic strain gradient. CP is particularly advantageous in capturing the intricate mechanics of material deformation by considering the emergence of plastic strain gradients arising from dislocation-based hardening laws. Their model distinctly considers the role of GNDs in accommodating lattice curvature and the movement of SSDs in inducing plastic deformation. Accordingly, the H trapping

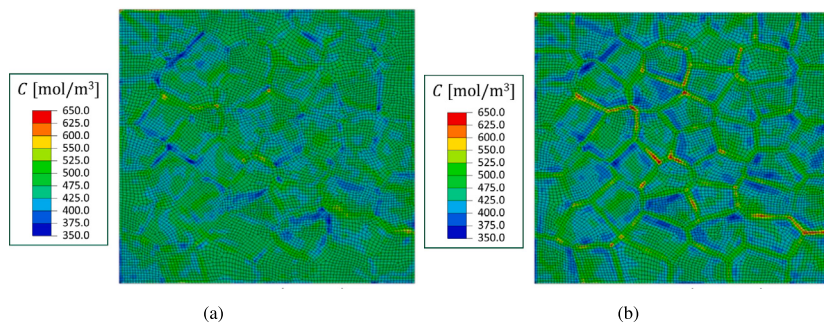


**Fig. 13.** Total H concentration  $C$  in polycrystalline RVE subjected to uniaxial tension for H transport (a) without mobile dislocation transport and (b) with mobile dislocation transport [145].

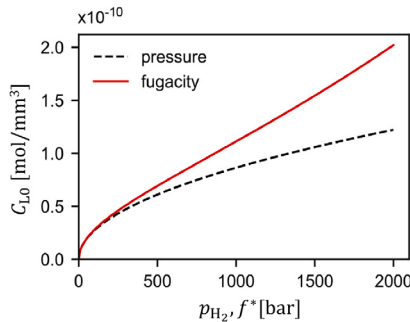


**Fig. 14.** The influence of gaseous H pressure  $p_{\text{H}_2}$  and fugacity  $f^*$  on the initial lattice concentration  $C_{L0}$  [116].

density  $N_T$  associated with dislocations on a particular  $\alpha$  slip system is defined in Yuan et al. [145] as,

$$N_T = \frac{\sqrt{3} \left( \sum_{\alpha}^{n_{\alpha}} (\rho_{SSD}^{\alpha} + |\rho_{GND}^{\alpha}|) \right)}{N_A b} \quad (41)$$

where  $N_A$  represents the Avogadro number,  $n_{\alpha}$  is the total number of slip systems and  $b$  is the magnitude of Burgers vector (shear vector). H transport by moving dislocations is then described by considering both the first-order H flux  $\mathbf{J}_{T,1}$  and second-order H flux  $\mathbf{J}_{T,2}$ ,

$$\mathbf{J}_D = \mathbf{R}^* (\mathbf{J}_{T,1} + \mathbf{J}_{T,2}) \quad (42)$$

where  $\mathbf{R}^*$  represents the orthogonal tensor denoting lattice rotation. The H flux  $\mathbf{J}_{T,1}$  drives H atoms from regions with a higher  $\theta$  to regions with a lower one, primarily related to plastic strain. On the other hand, the second-order H flux  $\mathbf{J}_{T,2}$  is determined by the evolution rates of GNDs densities, linked to the plastic strain rate gradient. Figs. 13(a) and 13(b) show the total H concentration  $C$  in polycrystalline RVE without mobile dislocation transport and with mobile dislocation transport [145]. A higher heterogeneity of H distribution is observed in the case of H transport with mobile dislocation as H migrates from grain interior to grain boundaries.

### 3.7. Influence of initial conditions

Besides specifying H uptake in the material boundaries and crack tip, accurate assumptions for initial conditions are also crucial. While assuming an initial zero H concentration holds for non-charged specimens [147], this assumption may not universally apply, particularly in studies involving precharged specimens where initial boundary conditions significantly affect HE predictions. In dry conditions without electrochemical reactions like corrosion [9,148], molecular H gas is the sole source of absorbable H atoms. Sieverts' law [149] has been

used in multiple studies [55,65,108,116,122,150–152] to explain the H concentration at NILS in thermodynamic equilibrium,

$$C_{L0} = k_L \sqrt{p_{\text{H}_2}} \quad (43)$$

where  $C_{L0}$  is the initial lattice H concentration,  $k_L$  is the Sieverts' constant (H solubility), and  $p_{\text{H}_2}$  is the partial pressure of molecular H. Eq. (43) is valid, assuming H gas does not behave ideally. The H solubility obeys an Arrhenius-type equation,

$$k_L = k_0 \exp \left( -\frac{H_T}{RT} \right) \quad (44)$$

where  $k_0$  is the constant and  $H_T$  is the enthalpy of a solution containing H. A H-fugacity  $f^*$  term can be used to modify the expression of Sievert's law given in Eq. (43) [56],

$$C_{L0} = k_s \sqrt{f^*} \quad (45)$$

where  $k_s$  is a solubility constant. H-fugacity  $f^*$  is a thermodynamic concept used to describe the effective pressure or escaping tendency of H gas in a given environment, and can be thought of as the “corrected” pressure that represents the thermodynamic activity of a gas. It is typically adopted at high H gas pressures and can be easily determined from measured pressure [116,153],

$$f^* = p_{\text{H}_2} \exp \left[ p_{\text{H}_2} \left( \frac{z_1}{T} + z_2 \right) \right] \quad (46)$$

where  $z_1$  and  $z_2$  are fitting coefficients which can be obtained from pressure-volume temperature (PVT) data using compressibility as a function of  $p_{\text{H}_2}$ . Fig. 14 shows the influence of gaseous H pressure  $p_{\text{H}_2}$  and fugacity  $f^*$  on the initial lattice H concentration  $C_{L0}$  [116].

## 4. Hydrogen-assisted deformation and fracture

H atoms diffuse within the lattice structure of metals and alloys, interacting with various microstructural features, thereby significantly influencing mechanical properties and fracture characteristics [13]. Accurately capturing this influence across different time and length scales poses a critical challenge in computational modeling. Various numerical investigations can be found in the literature on this topic, encompassing various coupled deformation-diffusion and deformation-diffusion-fracture approaches that provide capabilities to simulate the influence of H on material behavior. These methodologies include various theoretical models, continuum-based finite element simulations, state-of-the-art fracture modeling approaches, and micro-meso scale modeling frameworks such as DDD and CP.

### 4.1. Theoretical models

Initial developments in this area rely on simplified assumptions, focusing on specific quantitative aspects of the HE problem, such as critical fracture stress  $\sigma_c^*$ , critical flow stress  $\sigma_f^*$ , cracking threshold stress intensity factor (SIF)  $K_{\text{TH}}$ , and crack growth rate  $(da/dt)_{\text{II}}$  [3,98,154–159]. A critical fracture stress, denoted as  $\sigma_c^*$  is one of the common

description of HE adopted in these studies, which depends on the local H concentration  $C$  [112,154,155]. For example, in Akhurst and Baker [154], the fracture is assumed to occur over a critical distance in front of the crack tip once the crack-tip opening stresses exceed H-influenced critical fracture stress (or cohesive strength between metal atoms in FPZ). This relationship is often described linearly in many studies, as adopted in Akhurst and Baker [154],

$$\sigma_c^* = \sigma_0^* - \lambda C \quad (47)$$

where  $\sigma_0^*$  represents the fracture stress without the influence of H, and  $\lambda$  is a material-dependent constant. Akhurst and Baker [154] modeled subcritical cracking (i.e.,  $K_I = K_{TH}$ ) for gaseous H environments by relating the concentration of H in the unstressed region  $C_0$  to the external H pressure  $p_{H_2}$  using Sievert's law. In this context, the  $K_{TH}$  refers to a threshold value of the SIF below which H-induced crack growth is diminished, insignificant, or non-measurable. Considering the influence of hydrostatic stresses  $\sigma_H$ , the local H concentration  $C$  is defined as [154],

$$C \cong C_0 \exp\left(\frac{\tilde{V}_H \sigma_H}{3RT}\right) \quad (48)$$

Further extending this formulation, considering the analytical solution of the J2 plasticity in front of the stationary surface crack subjected to gaseous H pressure  $p_{H_2}$ , the expression for  $\sigma^*$  is modified as [154],

$$\sigma^* = \sigma_0^* - A(p_{H_2})^{1/2} \exp\left(\frac{2.6\sigma_{yy} - 1.3\sigma_{ys}}{3RT}\right) \quad (49)$$

where  $\sigma_{yy}$  is crack-tip tensile stress,  $\sigma_y$  is the yield stress, and  $A$  is an embrittlement factor. The model by Akhurst and Baker [154] predicts subcritical crack growth when the tensile stress exceeds the critical fracture stress  $\sigma_{yy} \geq \sigma_c^*$  over a critical distance  $x_c$  in front of the crack-tip. However, the predictions rely on correctly selecting parameters  $A$ ,  $\sigma_0^*$ , and  $x_c$ . Another model developed by Nair and Tien [156] to predict cracking threshold considers the critical flow stress  $\sigma_f^*$  based on the magnitude of stresses in front of the crack-tip,

$$\sigma_f^* = \sigma_f^0 + g' \left[ \frac{g_s b \sigma_c}{d_l} \right]^{1/2} \quad (50)$$

where  $g'$  is a geometric factor,  $\sigma_c$  is the cohesive strength,  $d_l$  is the dislocation pile-up length, and  $g_s$  is the shear modulus. H-assisted fracture is presumed to initiate when the flow stress exceeds a critical value over a critical distance. To overcome the drawbacks related to conventional J2 plasticity, Gerberich et al. [160] and Huang and Gerberich [159] proposed a mechanistic approach based on dislocation dynamics to describe the relationship between the threshold stress intensity  $K_{TH}$  and the H concentration in the FPZ  $C_{fpz}$  as follows,

$$K_{TH} \approx \frac{1}{\beta''} \exp \frac{(K_{IG} - \alpha' C_{fpz})^2}{\alpha'' \sigma_y} \quad (51)$$

where  $K_{IG}$  is the critical local fracture toughness (without the influence of H) as a function of surface energy  $\gamma_s$ , such that  $K_{IG} = \sqrt{2E\gamma_s}$ . The material parameters  $\sigma_y$  is the yield strength,  $E$  is the Young's modulus,  $\alpha'$  is a constant that captures the degradation of  $K_{IG}$ , and  $\alpha''$ , and  $\beta''$  are crack tip stress field constants which can be determined through finite element calculations by fitting with experimental results.

Many theoretical and numerical studies in the literature on crack behavior during HE have focused on intergranular fracture modes to represent the H-induced ductile-to-brittle transition in metals and alloys [65,161–166]. In these studies, the decohesion theory by Hirth and Rice [167] is particularly widely adopted, which describes the decohesion or separation at interfaces in the presence of a segregated solute using a thermodynamic approach. Hirth and Rice [167] applied the classical Gibbs adsorption isotherm to describe the separation process of interfaces, such as grain boundaries. Using their model [167,168], the reversible work of separation, or cohesive energy of an interface

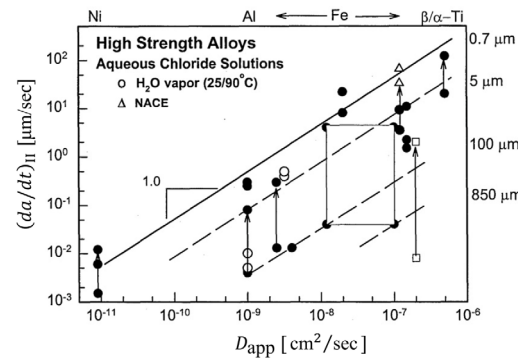


Fig. 15. Variation of stage II crack growth rate  $(da/dt)_{II}$  on  $D_{app}$  for high-strength alloys that exhibit H-assisted cracking in gases and electrolytes [3].

$2\gamma_{int}^H$ , in the presence of H for the case of fast separation (i.e., constant concentration) can be defined as [161],

$$2\gamma_{int}^H = (2\gamma_{int})_0 - (\Delta G_i^0 - \Delta G_s^0) \zeta \quad (52)$$

where  $\zeta$  is the interface coverage of H measured as solute atoms per unit reference interfacial area,  $\Delta G_i^0$  and  $\Delta G_s^0$  are the Gibbs energy of segregation for the interface and free surface, which can be obtained from the experimental adsorption studies, and  $(2\gamma_{int})_0$  is the cohesive energy for the H-free interface. Recently, Huang et al. [166] incorporated the thermodynamic decohesion model by Hirth and Rice [167] and provided a more concise form for  $K_{TH}$ , expressed in Eq. (51) [160], making it more practical and consistent with experimental data,

$$K_{TH} = \frac{1}{\beta''} (\beta'' K_{IC})^{(1-\eta'\theta_T)} \quad (53)$$

where  $\theta_T$  is the occupancy or fractional surface coverage of H at the interface,  $K_{IC}$  is the critical stress intensity factor or fracture toughness of the material, and  $\eta'$  is expressed as,

$$\eta' = \frac{(\Delta G_i^0 - \Delta G_s^0) \zeta_{max}}{(2\gamma_{int})_0} \quad (54)$$

where  $\zeta_{max}$  represents the maximum coverage of H at the interface.

Sofronis et al. [98] proposed a coupled theoretical framework to simulate the role of H in shear localization as per the HELP mechanism. The model incorporates the impact of H on material deformation through H-induced volume dilatation and material softening. H is assumed to exist in both NILS and reversible traps associated with plastic deformation. H-induced material softening is described by the decrease in flow strength  $\sigma_f$  under the presence of H in a continuum sense,

$$\sigma_f = \sigma_{y0}^H \left(1 + \frac{\epsilon}{\epsilon_0}\right)^{(1/m_p)} \quad (55)$$

where  $m_p$  is a strain hardening exponent,  $\epsilon$  is the logarithmic strain,  $\epsilon_0$  is the initial yield strain without the influence of H, and  $\sigma_{y0}^H$  is the yield strength with the influence of H,

$$\sigma_{y0}^H = QC\sigma_0 \quad (56)$$

The symbol  $Q$  represents a monotonically decreasing function in linear form as,

$$Q(C) = (\eta - 1)C + 1 \quad (57)$$

where  $\eta \leq 1$  is a material softening parameter.

Predicting stage II crack growth rate  $(da/dt)_{II}$  is considerably more complex than modeling cracking thresholds. This complexity arises from the need to comprehensively consider the numerous nuanced steps in the crack propagation process, particularly when making predictions encompassing a broad spectrum of environmental and mechanical parameters. In the context of HE, the  $(da/dt)_{II}$  represents

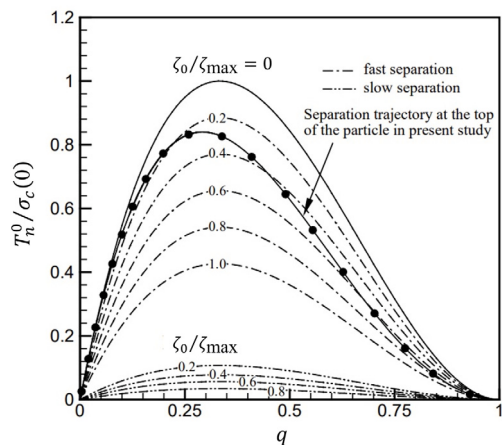


**Fig. 16.** Normalized interfacial traction  $T_n^0 / \sigma_c(0)$  as a function of interfacial separation  $q$  for the case of fast separation and slow separation at different interfacial H coverage  $\zeta_0 / \zeta_{\max}$  [162].

crack growth influenced by H diffusion, where the crack velocity is independent of SIF. To predict  $(da/dt)_{II}$ , many theoretical models employ a coupling mechanism between a transient unidimensional diffusion analysis along the cohesive ligament directly ahead of the crack tip [155,157,158]. In these studies [155,157,158], the cohesive force is assumed to degrade with the local H concentration. Subcritical crack growth occurs through successive incremental crack jumps, where equilibrium is re-established on the newly created crack surface after each jump. As an alternative, a generalized formalism was proposed in Gangloff [3] that unifies several diffusion-controlled models to estimate the  $(da/dt)_{II}$ ,

$$\left(\frac{da}{dt}\right)_{II} = \frac{D_{app}}{x_c} \left[ \xi \left( \frac{C_s}{C_{crit}}, D_H, x_c, \sigma_{ys}, t \right) \right] \quad (58)$$

where  $C_s$  is the H concentration at the crack surface,  $C_{crit}$  is the critical H concentration in the FPZ,  $x_c$  is a critical distance from the crack-tip,  $t$  is the time required for  $C_s$  to reach  $C_{crit}$  over the distance  $x_c$  and  $D_{app}$  is the apparent H diffusion coefficient, which is empirically derived from electrochemical H permeation tests permeation transient fitting techniques using metallic membranes [169]. Note that  $D_{app}$  is different from the effective diffusivity  $D_{eff}$ , which can be treated as an operational diffusivity due to an outcome of a mathematical rearrangement rather than a distinctive physical property [170]. The symbol  $\xi$  is the function of the different variables, as mentioned in Eq. (58), and provides output ranging from 0.01 to 4, depending on the model. Gangloff [3] conducted extensive experiments related to H environment-assisted cracking (HEAC) that provided valuable insights, demonstrating a nearly linear correlation between the measured stage II crack growth rates  $(da/dt)_{II}$  and the best available measured values of H diffusivity  $D_{app}$ . This correlation was observed across high-strength steels tested under various conditions, encompassing aqueous and gaseous environments (including  $H_2S$  and  $H_2$ ). The relationship between  $(da/dt)_{II}$  and  $D_{app}$  is shown in Fig. 15 highlights the significance of H diffusion in influencing crack growth rates.

#### 4.2. Continuum-based finite element simulations

FEM has arguably been the most widely used numerical tool over the last few decades across academia and industry. Likewise, FEM also played a pivotal role in various numerical investigations to investigate H-assisted deformation and fracture [65,113,162,171–176]. Liang and Sofronis [162] proposed a phenomenological traction separation law (TSL) to describe the constitutive cohesive behavior of an interface between inclusion and elastoplastically deforming matrix in continuum-based finite element calculations. The first part of

their work extends the H transport modeling framework of Sofronis et al. [98] and Krom et al. [56] to account for an additional H transport through an internally decohering interface. After that, following the decohesion theories of Hirth and Rice [167] and Rice and Wang [168] based on a thermodynamic approach, they provided expressions for cohesive strengths in decohesion, which were used to calibrate the cohesive model. Considering the work of separation as a function of the interfacial H segregation  $\zeta$  and the chemical potential  $\mu$ , two limiting scenarios were discussed, i.e., constant H concentration that characterizes brittle decohesion as rapid separation and constant H chemical potential that characterizes dislocation emission as slow separation. Liang and Sofronis provided the cohesive strengths for these limiting cases [162] as,

$$\sigma_c(\zeta) = \frac{16}{9\delta_n} [(2\gamma_{int})_0 - \zeta(\Delta G_i^0 - \Delta G_s^0)] \quad (59)$$

$$\sigma_c(\mu) = \frac{16}{9\delta_n} \left[ (2\gamma_{int})_0 - RT\zeta_{\max} \ln \left( \frac{[1 + (m-1)(\zeta_0/\zeta_{\max})]^2}{1 - (\zeta_0/\zeta_{\max})} \right) \right] \quad (60)$$

where  $\zeta_0 / \zeta_{\max}$  is the occupancy or fracture coverage of H at the interface (ratio of initial and maximum interfacial segregation of H at the interface), and  $m = \exp[(\Delta G_i^0 - \Delta G_s^0)/RT]$ . Fig. 16 show H-influenced phenomenological TSL for both limiting cases using their interfacial cohesion model, where  $T_n^0$  is the normal opening component,  $\sigma_c(0)$  is the maximum cohesive strength without the influence of H and  $q$  is a non-dimensional separation parameter, such that  $q = \sqrt{(u_n/\delta_n)^2 + (u_t/\delta_t)^2}$ . The relative displacement between points any two points that coincide before interface separation is represented by the symbols  $u_n$  and  $u_t$ , while the characteristic material constants for purely normal and tangential separation are denoted by the symbols  $\delta_n$  and  $\delta_t$ . The simulations in Liang and Sofronis [162] revealed that H could lower the threshold for plastic instability of materials, consistent with experimental observations. They also investigated how HEDE and HELP might work in tandem or in competition to support plastic localization or void nucleation.

Micromechanical models within the FEM framework offer a means to validate against experimental data, aiding in better predictions of deformation and fracture. For example, considering a HELP + HEDE mechanism, Novak et al. [65] proposed a coupled framework based on a statistical micromechanical fracture model and H diffusion model considering trapping at dislocations, carbides, and grain boundaries to study intergranular fracture in high-strength martensitic steel resulting from H charging. Their micromechanical fracture model is based on the physical mechanistic interpretation of the HE process adopted in their work, which attributes a twofold role to H. Firstly, it shields the stress between dislocations, consequently increasing the number of dislocations in pile-ups. Secondly, it reduces the reversible work required for interface separation, as H diminishes the strength of the carbide/matrix interface, thereby promoting fracture initiation at the carbide/matrix boundary. Their model predictions, as shown in Fig. 17 from the FEA-based fracture study on single-edged notched bending tests for steel specimens, reveal a strong agreement with experimental data.

SGP theory captures the local strengthening observed when the macroscopic strain field varies over microns, thereby leading to improved predictive capabilities for H concentration predictions and more accurate assessments of crack-tip mechanics due to strain gradient hardening [113]. To study H environment-assisted crack propagation threshold and kinetics using a coupled deformation-diffusion framework, Martinez-Paneda et al. [113] used SGP instead of finite strain J2 plasticity to model material behavior. They studied the role of GNDs through PSGP (refer to Section 3.4) and mechanism-based strain gradient plasticity (MSGP), integrating continuum scale plasticity and discrete dislocation modeling. To implement MSGP, a Taylor dislocation model is adopted, which relates the shear flow strength  $\sigma_f$  of the material to the total dislocation density  $\rho$  [135]. Assuming small

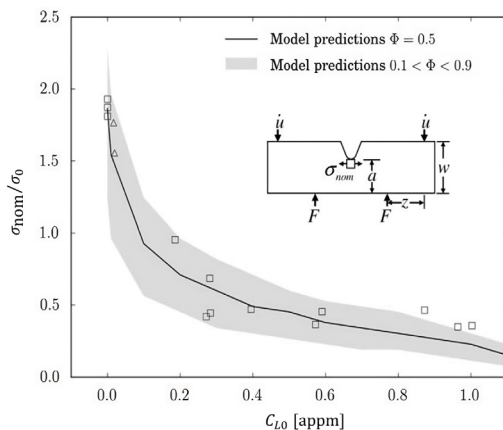


**Fig. 17.** Variation of normalized bending stress ( $\sigma_{\text{nom}}/\sigma_0$ ) as a function increasing initial H concentration  $C_{L0}$  in the NILS [65].

dislocation densities,  $\rho_{\text{GND}}$  can be related to the curvature of plastic deformation as [113,177],

$$\rho_{\text{GND}} = \bar{r} \frac{\eta^p}{b} \quad (61)$$

where  $\eta^p$  is the gradient of equivalent plastic strain  $\epsilon_p$ ,  $\bar{r}$  is the Nyce-factor which is a scalar measure of  $\rho_{\text{GND}}$  in case of 3D non-uniform plastic deformation (around 1.90 for fcc crystals), and  $b$  is the magnitude of Burgers vector. The MSGP relationships predict  $\sigma_f$  as [114],

$$\sigma_f = \sigma_{\text{ref}} \sqrt{[f(\epsilon_p)]^2 + h\eta^p} \quad (62)$$

where  $h$  is an intrinsic material length scale in SGP,  $\sigma_{\text{ref}}$  is a reference stress, and  $f$  is a non-dimensional function of  $\epsilon_p$  based on a power-law strain-hardening law,

$$f(\epsilon_p) = \left(1 + E \frac{\epsilon_p}{\sigma_y}\right)^{m_p} \quad (63)$$

where  $m_p$  is a strain-hardening exponent and  $E$  is Young's modulus. The detailed FEM implementation of both PSGP and MSGP in a finite-strain crack-tip problem is provided in [178,179]. The cracking threshold  $K_{\text{TH}}$  is computed using Eq. (51), following the approach by Gerberich et al. [155], where the constants  $\beta'$  and  $\alpha''$ , are determined from computer simulations assuming dislocation shielding [180], and the local H concentration to be used as input is computed as,

$$C_{\text{fpz}} = \left[ C_L \frac{1 - C_{L\sigma}}{1 - C_L} \exp\left(\frac{\sigma_H \tilde{V}_H}{RT}\right) \right] \left[ 1 + \frac{1 - C_T}{1 - C_L} \exp\left(\frac{E_b}{RT}\right) \right] \quad (64)$$

where  $C_L$  is the H concentration in NILS due to lattice dilation and  $C_T$  is the H concentration in the reversibly trapped for a single trap site. The numerical predictions in Martinez-Paneda et al. [113] (both  $K_{\text{TH}}$  and stage II crack growth rate ( $da/dt$ )<sub>II</sub>) agree well with experiments, where gradient-enhanced calculations reveal substantial H concentrations within the critical distance of H-assisted fracture, rationalizing HEDE mechaism. Fig. 18(a) shows the FEA-computed normalized  $\sigma_H/\sigma_Y$  ahead of the crack-tip using MSGP, PSGP, and classical von Mises plasticity, highlighting the profound impact of SGP, noticeably visible in the crack-tip stresses. Note that the crack-tip hydrostatic stress distribution for these cases in Fig. 18(a) is computed for several applied  $K_I$  where the H-assisted fracture occurred. Fig. 18(b) illustrates a good quantitative agreement between the FEA-computed  $K_{\text{TH}}$  using Eq. (51) for  $\sigma_H$  determined by MSGP and PSGP and experimental measurements for Monel K-500 at applied potential  $E_{APP}$  of -1.000 V.

#### 4.3. State-of-the-art fracture models

Over the last two decades, various advancements have taken place in new fracture modeling approaches, leading to the development of

a range of new deformation-diffusion-fracture models that integrate H diffusion, deformation, and fracture. In particular, the application of state-of-the-art crack modeling approaches, such as cohesive zone modeling (CZM), gradient damage models (GDM), phase field (PF) models, and peridynamics (PD), have been widely adopted in these developments.

##### 4.3.1. Cohesive zone models

Most conventional modeling approaches describe H distribution concerning stationary notches or cracks. However, CZM offers numerical capabilities to describe H distribution in connection with a propagating crack. The key idea is to introduce cohesive interface elements along a known crack path whose material behavior is governed by a traction separation law (TSL) or a cohesive law. Fig. 19 show the commonly used TSLs used in the literature [181] that provide a macroscale description of the micromechanical material behavior in the FPZ. The initial idea behind CZM can be traced back to Dugdale [182] and Barenblatt [183], which has since been extended to various other problems, including HE [91,108,150–152,165,184–192]. In its simplest form, the critical cohesive stress is assumed as a linear function of H concentration, given by,

$$\sigma_c(C) = \sigma_c(0)(1 - \eta C) \quad (65)$$

where  $\sigma_c(0)$  is the critical cohesive stress without the influence of H, and  $\eta$  is a softening parameter often that can be obtained by fitting the results from experimental data.

Serebrinsky et al. [91] is one of the earliest noteworthy contributions introducing CZM to simulate H-assisted fracture, which incorporates a time-dependent coupling between stress-assisted Fick's law-governed H mass transport and local degradation of the cohesive zone in front of the crack. The cohesive elements are governed using a linear atomic-level TSL, inferred from the first principles calculations of van der Ven and Ceder [194] and Jiang and Carter [195]. In the case of Jiang and Carter [195], a periodic density function theory (DFT) approach is adopted to estimate the ideal fracture energy for metals, such as Fe and Al, which is used as an input in multiple numerical investigations on H-assisted fracture. [91,92,184–186]. Ab initio (from first principles) simulations based on DFT replicate complex H-metal interactions, providing fundamental insights into multiple HE mechanisms through quantum mechanics-based considerations, especially the interactions between H and defects in a material microstructure, which can be used as input at the continuum scale. To capture H-induced degradation, the surface fracture energy is linked to local H occupancy  $\theta_T$  at grain boundaries, as per the DFT calculations of Jiang and Carter [195] as,

$$\gamma(\theta_T) = q\gamma(0) \quad (66)$$

where  $\gamma(0)$  is the fracture energy of the surface without H and  $q = 1 - 1.0467\theta_T + 0.1687\theta_T^2$ . Similar to Eq. (66), the cohesive stress related is defined as [91],

$$\sigma_c(\theta_T) = q\sigma_c(0) \quad (67)$$

where  $\sigma_c(0)$  is the cohesive stress without the influence of H. The hydrostatic stress driving H transport is calculated from static stress analysis considering J2 elastoplasticity with power-law strain hardening. Microstructural trap sites also affect H diffusion, which is reflected in the effective diffusivity coefficient  $D_{\text{eff}}$ . Fig. 20(a) shows the influence of  $\theta$  on normalized cohesive law, adopted in Serebrinsky et al. [91]. Whereas, Fig. 20(b) presents the variation of the normalized  $K_{\text{TH}}$  and normalized  $\sigma_c$  as a function of H concentration  $C$ , based on a linear H-dependence relation in Eq. (65) and H-dependence used in Eq. (67) adopted by Serebrinsky et al. [60,91].

Olden et al. [184,185] used weakly-coupled stress-diffusion models to predict H-assisted fracture in stainless steel, adopting an H-induced fracture energy degradation inferred from the work of Jiang and Carter [195] and Serebrinsky et al. [91]. A more advanced version

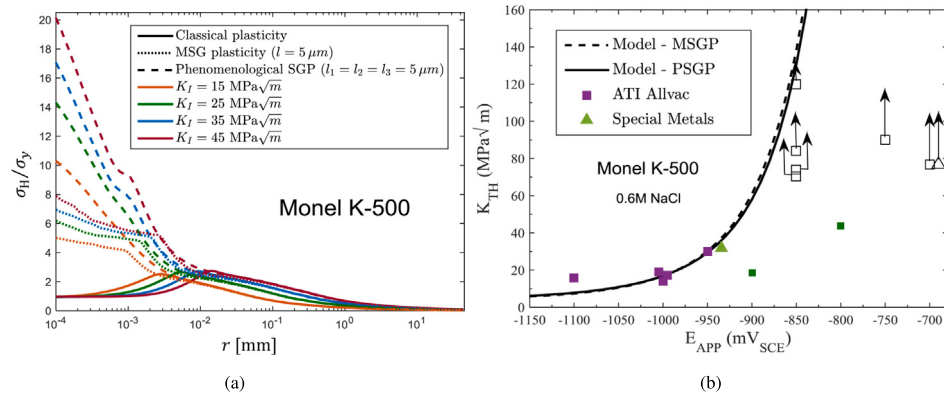


**Fig. 18.** (a) FEA-computed  $\sigma_H/\sigma_Y$  in front of the crack-tip for Monel K-500 [113], (b) Comparison between FEA-computed and experimental data of  $K_{\text{TH}}$  at applied potential  $E_{\text{APP}}$  of  $-1.000 \text{ V}$  [113].

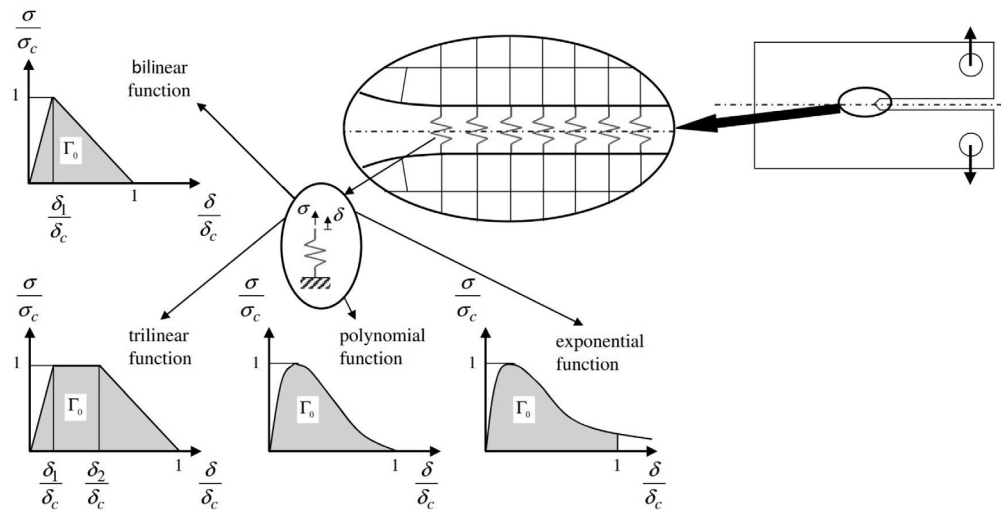


**Fig. 19.** Commonly used traction separation laws in CZM models [181].

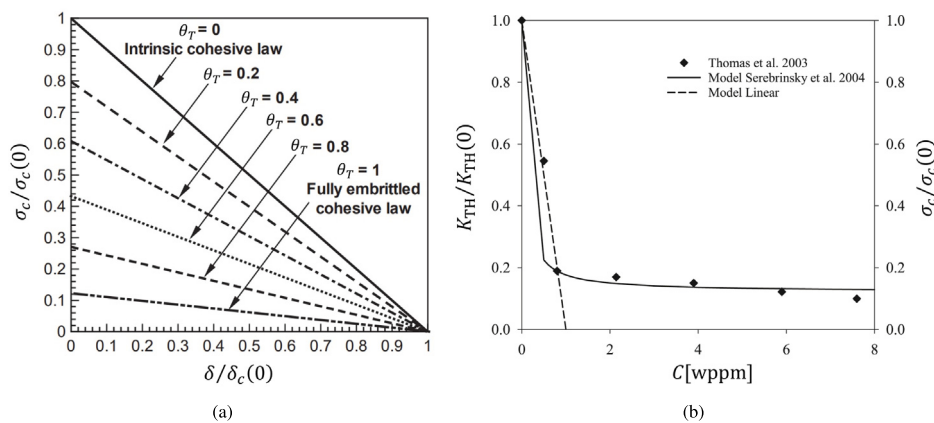


**Fig. 20.** (a) Influence of trapped H occupancy  $\theta_T$  on normalized TSL cohesive law adopted in Serebrinsky et al. [91], (b) Normalized threshold stress intensity  $K_{\text{TH}}$  and cohesive stress  $\sigma_c$  as a function of H concentration  $C$  [60,91,193].

of this approach is implemented in Alvaro et al. [150,196] in 3D, where a CZM modeling approach is adopted to capture HE in X70 pipeline steel. Fig. 21 illustrates a detailed flowchart of the three-step modeling procedure adopted in Alvaro et al. [150,196] to capture HE. A polynomial TSL is adopted to govern the constitutive behavior of the cohesive elements. In Alvaro et al. [186], DFT calculations based

on Jiang and Carter [195], nanoscale experiments and FEM are combined to study the influence of H and grain boundary misorientation on intergranular fracture. The integrated approach employs CZM-FE simulations at the continuum scale and DFT calculations [195] at the atomistic scale to incorporate the effect of H on the cohesive strength of grain boundaries. A bilinear TSL is adopted to simulate decohesion

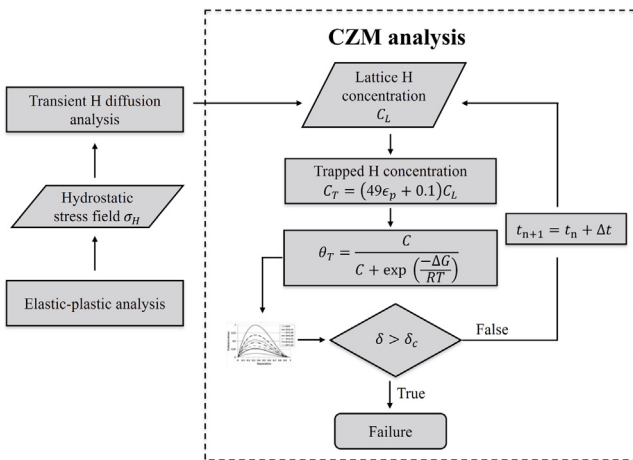


Fig. 21. Flowchart of modeling procedure for prediction of HE [150].

using CZM, considering nanosized Ni bi-crystal cantilever beams. The ideal fracture energy to be used as input to the CZM model is defined as [195],

$$2\gamma = \frac{E_{\text{crack}}^{\text{GB+xH}} - E_{\text{GB+xH}}^{\text{uncrack}}}{2A} \quad (68)$$

where  $A$  is the area of the grain boundary plane ( $2A$  represents the total area of the surfaces), and  $E_{\text{GB+xH}}^{\text{crack}}$  and  $E_{\text{GB+xH}}^{\text{uncrack}}$  are the energies of the grain boundary with  $xH$  atoms after and before cracking. The fracture energy obtained using the relation given in Eq. (68) is related to  $\theta_T$  to incorporate the influence of H for input to the FEM simulations. Fig. 22(a) illustrates the calculated degradation in ideal fracture energy using DFT simulations with increasing  $\theta_T$  along planes (111 and 012) in bulk Ni and low angle and low coincidence grain boundaries in pure Ni ( $\Sigma 3$  and  $\Sigma 5$ ) [186]. Notably, the grain boundaries exhibits a higher decohesion strength reduction than the same planes in bulk Ni. Fig. 22(b) illustrate the numerical results of FEM simulations in a Ni bi-crystal system ABAQUS cohesive simulations for the cantilever beam for the  $\Sigma 3$  and  $\Sigma 5$  misorientation. The  $\Sigma 5$  grain boundary exhibits a more significant reduction in strength compared to the  $\Sigma 3$ , highlighting the role of grain boundary misorientation on the mechanical response.

Lin et al. [191] proposed a general computational modeling framework to simulate ductile-to-brittle transition (DBT) in metals, where a complete Gurson model (CGM) [197] is adopted to simulate ductile fracture and CZM for brittle fracture. A polynomial TSL governs the constitutive response of the cohesive elements, where stress  $\sigma_c(\delta)$  for the separation  $\delta$  is expressed as,

$$\sigma_c(\delta) = \begin{cases} \frac{27}{4} \sigma_c \frac{\delta}{\delta_c} \left(1 - \frac{\delta}{\delta_c}\right)^2 & \delta \leq \delta_c \\ 0 & \delta \geq \delta_c \end{cases} \quad (69)$$

where  $\sigma_c$  is the cohesive strength of the cohesive elements and  $\delta_c$  is the critical separation. The H-induced degradation is captured using the relation given in Eq. (67) where  $\sigma_c$  is a function of trapped H occupancy  $\theta_T$  for a H/Fe system [91,195]. A virtual tensile test simulation is performed to simulate HE considering material models, where the proposed framework captures both types of fractures and their competition to simulate DBT. Fig. 23(a) highlights the role of H on the engineering stress versus true strain. Similarly, Fig. 23(b) shows the variation of failure strain  $\epsilon_f$  as a function initial H concentration  $C_{L0}$  considering two different material models M1 ( $f_0 = 0.001$ ,  $\sigma_y = 400$  MPa,  $m_p = 0.1$ ) and M2 ( $f_0 = 0.001$ ,  $\sigma_y = 400$  MPa,  $m_p = 0.15$ ), where  $f_0$  is the initial void volume fraction,  $\sigma_y$  is the yield strength and  $m_p$  is the hardening exponent. Notably, the experimental results exhibits similarity with the experimental observations, where failure strain show a sudden drop after a critical H concentration due to DBT.

#### 4.3.2. Gradient damage models

Smeared crack modeling approaches are gaining more traction among researchers due to their relative ease of implementation and their ability to handle complex cracking scenarios [200,201]. In one such application to HE, Anand et al. [109] proposed a coupled deformation-diffusion-damage theory as an extension to their previous work [103,111] to simulate crack growth in medium-strength ferritic steels, following the observations from experimental investigations in Xu and Rana [198]. The coupled framework adopts gradient damage modeling (GDM) approach to simulate damage or craze-breakdown and final fracture. It introduces a scalar damage field  $d$  and its spatial gradient  $\nabla d$ , similar to the PF approach (to be discussed later). A scalar damage field  $d \in [0, 1]$  provides a smeared description of H-assisted crack growth, which varies from 0 to 1, such that 0 represents a completely intact state at a material point, and 1 represents complete failure. The inelastic deformation within coupled framework is referred to as craze inelasticity, and the strain produced by crazing is called a quasi-brittle form of inelastic deformation. The model is implemented within a FEM framework through an element subroutine code in the software platform ABAQUS. Fig. 24(a) and (b) present a comparison of tensile stress-strain curves and tensile elongation (failure strain  $\epsilon$ ) with the experimental data of the tension test, highlighting a quantitative correlation that exists between the numerical results and the experimental results. Fig. 25 illustrates the evolution of craze strain  $\epsilon^c$  for the loading points a, b, c and d marked using red markers in Fig. 24(a), which starts with accumulation at the middle plane, followed by the initiation and growth of a H-assisted fracture.

#### 4.3.3. Phase field models

Over the last two decades, PF formulations have become a promising computational tool to simulate fracture with applications to various engineering problems. They belong under variational approaches to fracture, where a sharp crack is geometrically regularized into a narrow band of intense damage using an internal length scale. The crack growth is tracked implicitly through an auxiliary scalar phase field variable  $\phi \in [0, 1]$ , following the path of least energy. A phase field variable  $\phi$ , similar to a damage variable  $d$  (refer to Section 4.3.2), describes the extent of damage at a material point, such that 0 represents a completely intact state, and 1 represents complete failure. Recently, PF models have been applied in numerous works to investigate the H-assisted fracture and fatigue [92,99,104,104–106,202–210]. In one of the earliest works, Duda et al. [104] coupled elastoplastic deformation, PF fracture, and H migration to capture subcritical crack growth in solids. To couple a PF description of fracture with material deformation and H diffusion, an additional phase field micro-force balance is introduced, which leads to the following set of governing equations for the phase field  $\phi$  obtained by combining force balances and the constitutive theory,

$$\begin{aligned} \dot{\phi} &\geq 0, W \leq 0, \dot{\phi}W = 0 \\ W &= 2(1-\phi)\psi_0 - G_c \left( \frac{1}{l}\phi - l\nabla\phi \cdot \nabla\phi \right) \end{aligned} \quad (70)$$

where  $W$  is a phase field loading function,  $G_c$  is the critical strain energy release rate and  $\psi_0$  is elastic free energy density for an undamaged solid. HE is captured using the following relation, which relates  $G_c$  to the  $\theta_T$  associated with microstructural traps as,

$$G_c = G_c(0)(q)^{p_e} \quad (71)$$

where  $G_c(0)$  is the critical strain energy release rate without the influence of H,  $q$  is a function of  $\theta_T$  that captures H-induced degradation of  $G_c(0)$ , and  $p_e$  is an exponent, which can be calibrated to correlate with the experimental results. In Duda et al. [104], the  $q = (1 - 1.0467\theta_T + 0.1687\theta_T^2)$  is assumed from the work of Serebrinsky et al. [91], where  $\theta_T$  is calculated following the Langmuir–McLean isotherm relation provided in Eq. (19). The coupled PF formulation by Duda et al. [104] captures both material deformation and fracture due to the influence of

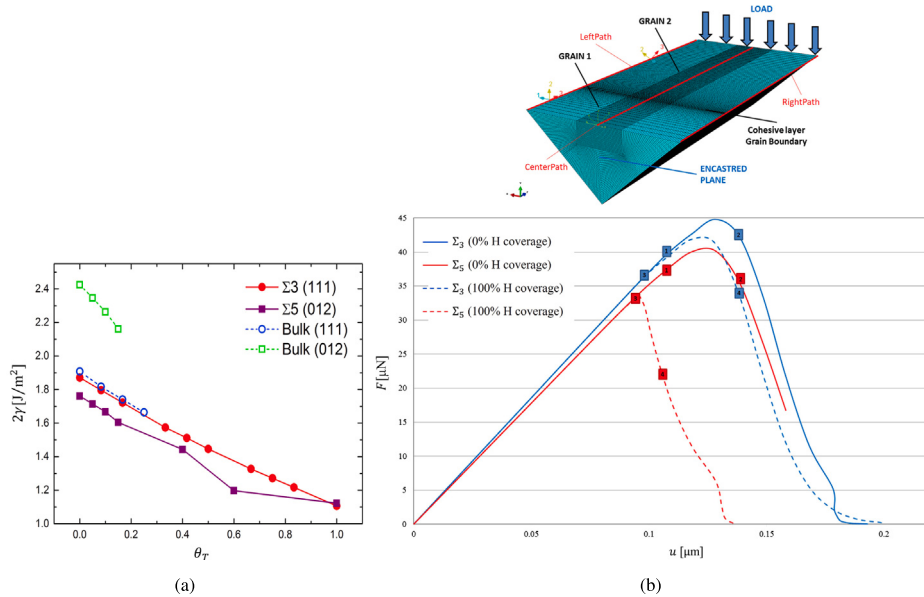


**Fig. 22.** (a) Ideal fracture energy as a function of trapped H occupancy  $\theta_T$  for planes (111) and (012) for bulk Ni and grain boundaries ( $\Sigma_3$  and  $\Sigma_5$ ), (b) Influence of H on the load–displacement response of the bi-crystal cantilever beam for  $\Sigma_3$  and  $\Sigma_5$  misorientation [186].

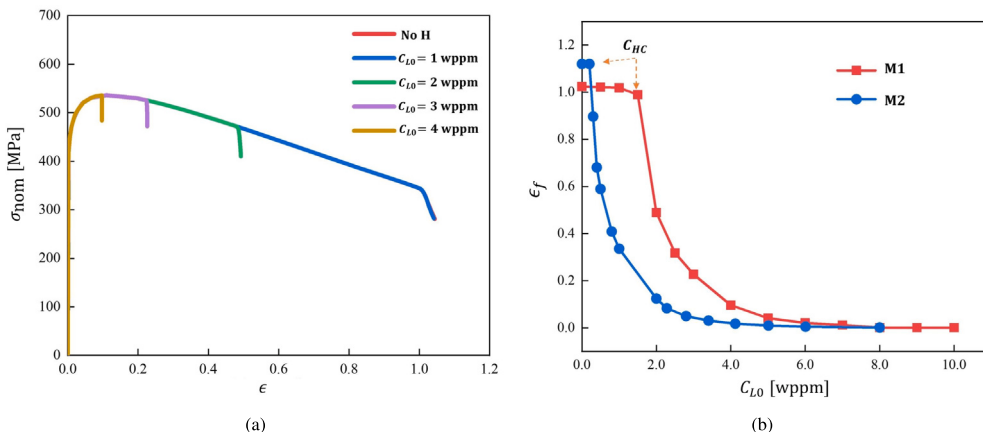


**Fig. 23.** (a) Engineering stress  $\sigma_{\text{nom}}$  as a function of true strain for different initial H concentration  $C_{L0}$ , (b) Failure strain  $\epsilon_f$  as a function of initial H concentration  $C_{L0}$  for material models M1 and M2 [191].

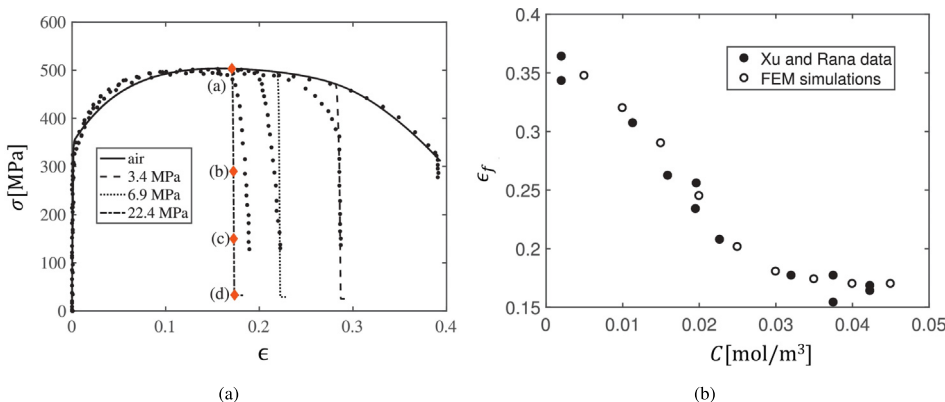


**Fig. 24.** (a) Numerical (dashed lines) and experimental (dotted lines) tensile stress–strain  $\sigma$  –  $\epsilon$  curves at different H pressures, (b) Tensile elongation (failure strain  $\epsilon_f$ ) as a function of H concentration  $C$  [109,198].

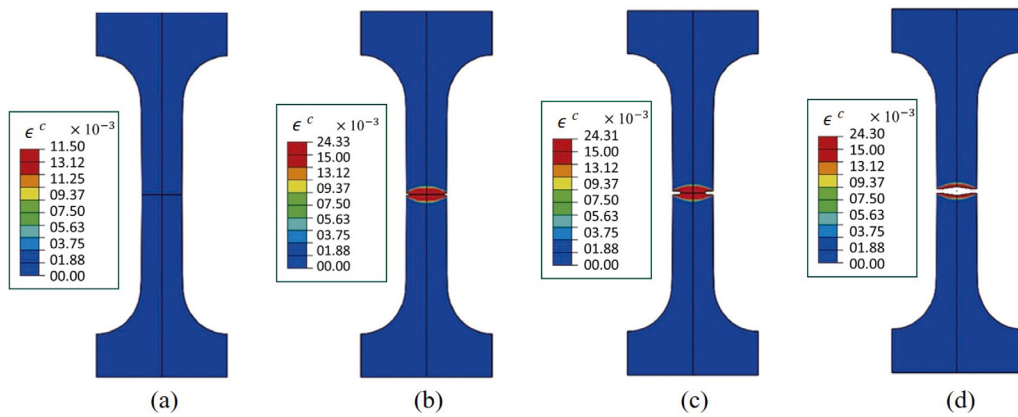


**Fig. 25.** Evolution of craze strain  $\epsilon^c$  (crack growth is illustrated by removing the finite elements with  $d \sim 1$ ) [109].

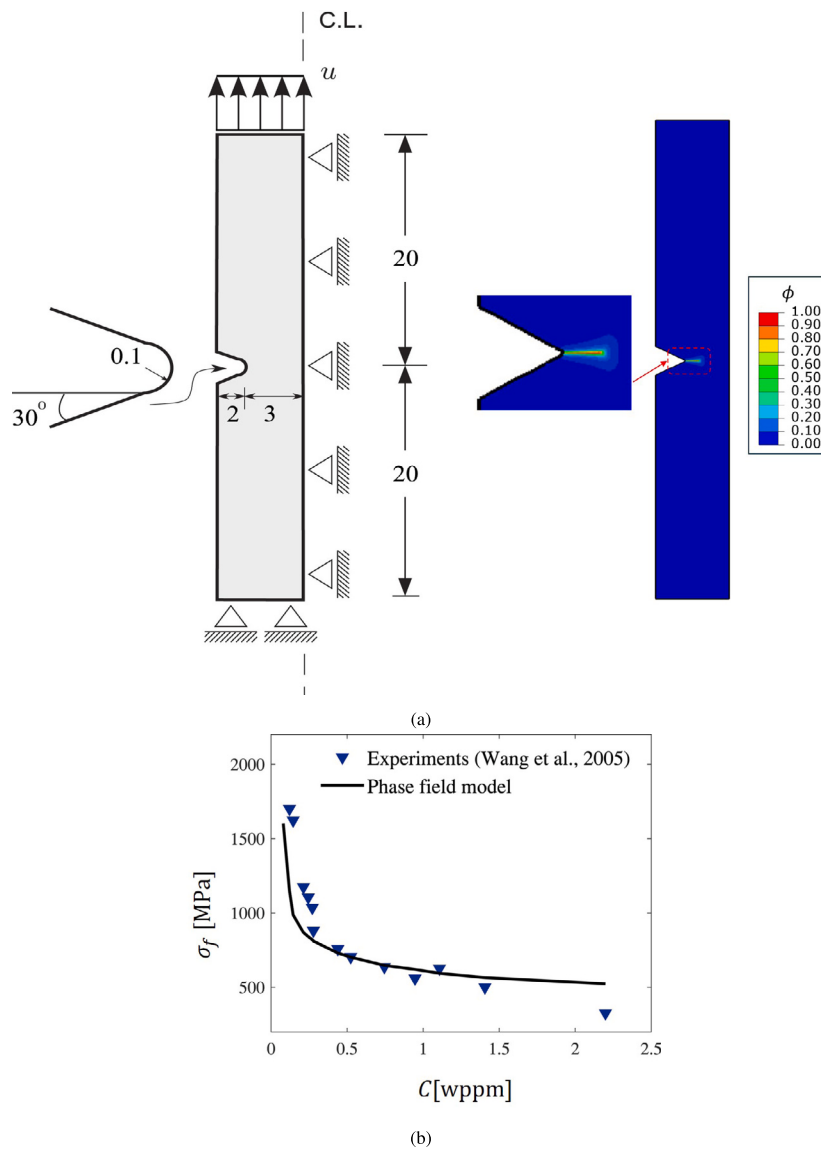


**Fig. 26.** (a) PF ( $\phi$ ) evolution and growth in a notched tensile bar, and (b) Net section strength  $\sigma_f$  as a function of H concentration  $C$  [92] (comparison with the experimental results [199]).

H, and their numerical results qualitatively correlated well with prior numerical works.

A similar PF-based coupled theoretical framework is proposed in Martinez-Paneda et al. [92] to predict H-assisted fracture by taking the fracture energy as a function of H occupancy at trap sites, inspired by the first-principles calculations. A linear relation between  $G_c$  and  $\theta_T$  is assumed to capture H-induced material degradation,

$$G_c(\theta_T) = (1 - \kappa\theta_T)G_c(0) \quad (72)$$

where  $\kappa$  is a damage coefficient that captures the effect of H due to HE, deduced from DFT calculations. Additionally, the effect of H trapped at microstructural sites and its influence on H transport is considered using an apparent diffusion coefficient  $D = D_{app}$ . Both qualitatively and quantitatively, the PF predictions of Martínez-Pañeda et al. [92] (failure stress,  $K_{TH}$ , and crack growth patterns), correspond well with the experiments. Fig. 26 (a) shows the crack growth profile in the notched tensile specimen obtained, described by the PF variable  $\phi$ . Fig. 26(b) illustrates a comparison between the failure stress (net section stress) obtained in experiments for steel [199] to the numerical results [92]. Huang and Gao [99] proposed a coupled deformation-diffusion-fracture framework to simulate HE at a continuum scale, considering both HELP and HEDE mechanisms, by incorporating the fracture energy and yield strength as the function of H concentration.

Kristensen et al. [202] proposed a coupled PF formulation integrating stress-assisted H diffusion, SGP, and PF fracture to simulate HE comprehensively. Their findings provide intricate insights into the interplay of various factors influencing HE, particularly emphasizing the crucial role of plastic strain gradients in elucidating de-cohesion-based phenomena. The model successfully captures the ductile transition to brittle fracture observed in H-containing environments due to the correct prediction of large crack-tip stresses. These high stresses elevate the H concentration and concurrently diminish the fracture energy, contributing to the mechanistic understanding of HE-induced brittle fracture. Furthermore, PF models have been effectively employed in applications to predict H-influenced fatigue crack growth rates and S-N curves in virtual laboratory experiments [203]. Some representative results depicted in Fig. 27 showcase PF modeling capabilities via virtual tests on structural elements like screw anchors and corroded pipelines with internal defects. These simulations consider diverse combinations of material properties, environmental conditions, and loading scenarios, providing a comprehensive investigation of HE effects on the structural integrity of different structural elements.

There has been an increase in computational studies based on different fracture modeling approaches to capture intergranular and transgranular fracture modes in polycrystalline materials while explicitly considering the underlying microstructure [212–215]. A noteworthy contribution as an extension to the study HE comes from Valverde-González et al. [211], where a microstructure-sensitive coupled deformation-diffusion-fracture model is proposed. Fig. 28(a) provides a comprehensive overview of the modeling methodology employed by Valverde-González et al. [211], that integrates a CZM to describe the failure of grain boundaries and transgranular crack propagation based on the variational PF approach associated with ductile fracture processes. Their integrated approach explicitly captures the intricate interactions between H and microstructure, shedding light on the interplay between transgranular and intergranular fracture mechanisms. Fig. 28 presents the results from one of their benchmark problem to simulate fracture in a single-edge notched plate comprising 50 grains. The model captures the degradation in material response and the shift in cracking patterns from a transgranular fracture mode to an intergranular with increasing H concentration. One of the key highlights of their work was a virtual slow strain rate test (SSRT) test on a Ni-Cu superalloy (Monel K-500), where the numerical results exhibited qualitative and quantitative agreement with the experimental results.

#### 4.3.4. Peridynamics

In addition to PF models, HE has been modeled in multiple recent numerical investigations using peridynamics (PD), a novel non-local approach [217–219]. PD is a robust nonlocal reformulation, a recently developed theory in solid mechanics that employs integral-differential equations, making it suitable for modeling nucleation and growth of cracks. The continuum is subdivided into material elements within a PD framework, which are connected through physical interactions denoted as bonds and their stiffness. Following the Griffith theory, the concept of failure is introduced by allowing the bonds to rupture whenever they are extended beyond a predetermined limit, known as a critical stretch threshold or critical elongation  $s_0$ , computed using the bond's fracture energy. For applications to simulate fracture, Chen et al. [220] proposed the initial iteration of a PD framework for simulating the detrimental effects of corrosion in an environment, using a stochastic relation between the concentration in the metal and the damage at the mechanical bonds. Expanding PD applications to HE, De Meo et al. [218] recently proposed a theoretical framework coupling PD with H diffusion to capture stress-corrosion fracture in high-strength steels, considering the AIDE mechanism. Within the PD framework, the trapped H occupancy  $\theta_T$  is defined as [218],

$$\theta_T = \frac{C}{C_{sv}} \quad (73)$$

where  $C$  represents the H concentration at the crack-tip and  $C_{sv}$  is its saturated value. The material damage (defined by bond breakage) occurs when the stretch (elongation of the bond) is greater than a critical value, defined as that critical bond stretch (or critical elongation)  $s_0$ ,

$$s_0 = \sqrt{\frac{10G_c}{\pi c \delta_l^5}} \quad (74)$$

where  $G_c$  is the critical energy release rate or fracture energy of the bond,  $c$  is a micro-modulus parameter, and  $\delta_l$  refers to the horizon size within the framework of PD. To capture H-induced degradation,  $s_0$  is related to the  $\theta_T$ , based on the fit of data from the first principle calculations of Jiang and Carter [195] in Serebrinsky [91],

$$s_0(\theta_T) = s_0(0)(1 - 1.0467\theta_T + 0.1687\theta_T^2) \quad (75)$$

where  $s_0(0)$  refers to the value of critical bond stretch without the influence of H, computed from Eq. (74). Their numerical results reveal a good agreement between the experimental and numerically obtained crack growth rates for different loading conditions. Recently, Ran et al. [217] extended the coupled framework of De Meo et al. [218] to simulate H-assisted fracture in low alloy steels, considering the AIDE mechanism for HE. The approach couples PD H diffusion, considering the role of temperature. Fig. 29(a) illustrates the evolution of crack growth and H occupancy  $\theta_T$  at different load steps at a temperature of 400°C, obtained using PD simulations. The numerical results exhibit a good resemblance to the experimental observations [216] (see Fig. 29(b)), indicating that elevated temperature promotes the permeation of H within the material.

#### 4.4. Micro-meso scale investigations

While atomistic-scale simulations furnish intricate insights, their computational overheads and limitations render them unsuitable for probing the effect of H at microstructure and component scale. Recently, attention has turned to advanced micro-mesoscale investigations employing physics-based frameworks like DDD and CP to better understand HE phenomena at scales relevant to real-world materials and structures.

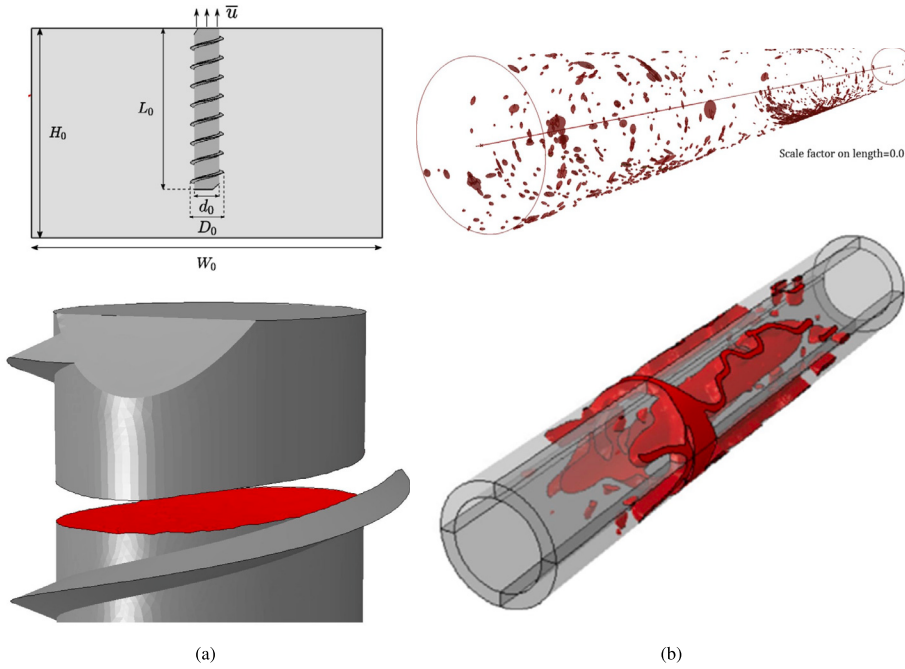


**Fig. 27.** (a) PF modeling of a virtual test in a screw anchor undergoing HE, and (b) PF modeling of fracture in a corroded pipeline with pre-existing internal defects (measured via inline inspection) undergoing HE [203].

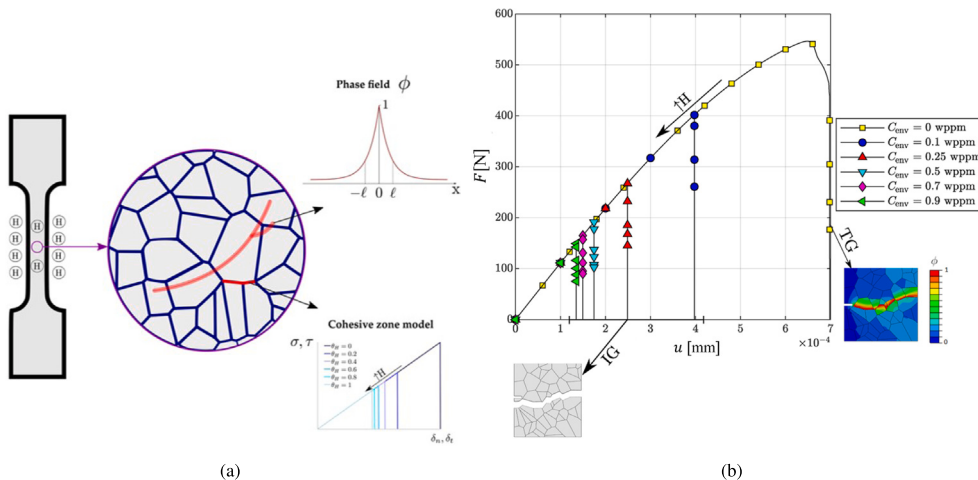


**Fig. 28.** (a) Modeling framework in Valverde-González et al. [211] to simulate ductile transgranular crack growth and H-assisted grain boundary decohesion, and (b) Load-displacement ( $F - u$ ) of a 50-grain single-edge notched plate for various environmental H concentrations [211].

#### 4.4.1. Discrete dislocation dynamics simulations

DDD has emerged as a popular approach to simulate dislocation-mediated plasticity in metals and the emergent fracture behavior associated with dislocation evolution at the mesoscale. Compared to ab initio and molecular dynamics (MD) simulation methods, DDD simulations are less computationally restrictive as they average out the atomistic details and offer capabilities to study the collective dynamics of large dislocation (i.e., a kind of line defect) ensembles explicitly by treating individual dislocation segments as discrete entities within a crystal lattice along with their interactions [221–223]. MD is a widely used computational simulation technique that studies the time evolution of interacting atoms and molecules by integrating their equations of motion, providing valuable insights across various scientific and engineering disciplines [224]. Fig. 30 presents a schematic representation of dislocation segments in 2D DDD simulations of infinitely long edge dislocations and curved lines in 3D DDD simulations. Recently, the applications of DDD simulations have been extended to simulate

the influence of H on the collective behavior of dislocations and even quantitatively describe different HE mechanisms [225–228].

Gu and El-Awady [226] proposed a comprehensive 3D DDD framework to study the shielding effect of H on the dislocation field at the mesoscale by coupling H-dislocation interactions and bulk H diffusion. An analytical formulation is developed for the H-induced stress field  $\sigma^H$  in 3D space built upon the 2D formulation in [230], based on the assumption that H concentration is in equilibrium with the pre-existing dislocation stress field. The equilibrium H distribution follows Fick's law of H diffusion expressed in Eq. (5), where the equilibrium lattice H occupancy  $\theta_L$  is defined as,

$$\theta_L = \left[ 1 + \frac{1 - \theta_{L0}}{\theta_{L0}} \exp\left(\frac{W_{int}}{k_B T}\right) \right]^{-1} \quad (76)$$

where  $\theta_{L0}$  is the reference lattice H occupancy at NILS,  $k_B$  is the Boltzmann constant,  $W_{int}$  is H-dislocation interaction energy. Following the Eshelby inclusion model, a first-order elastic interaction energy

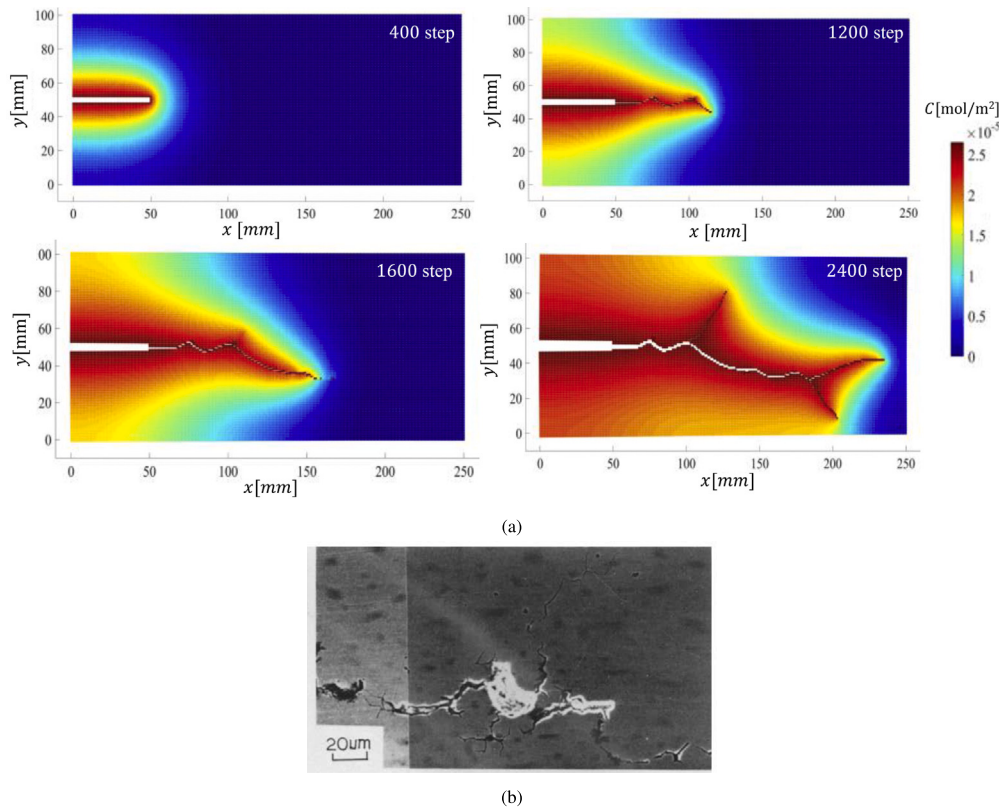


**Fig. 29.** (a) Crack growth evolution and H concentration  $C$  at different steps, and (b) SEM image of the sample surface [216,217].

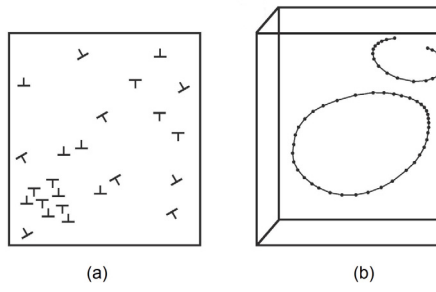


**Fig. 30.** Schematic representation of dislocation segments in 2D DDD simulations and 3D DDD simulations dislocation loops discretized by linear segments [229].

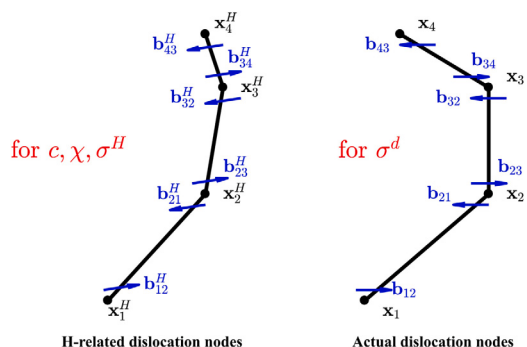


**Fig. 31.** Schematic illustration of H-related dislocation nodes and actual dislocation nodes [226].

term for the H-dislocation interaction in the presence of a dislocation stress field  $\sigma^d$ ,

$$W_{int} = P \Delta V \quad (77)$$

where  $P$  is the hydrostatic stress associated with  $\sigma^d$  and  $\Delta V$  is the extra volume of solute H associated with the partial molar volume of H. Within the 3D DDD framework, dislocations are discretized into connected straight segments with endpoints as dislocation nodes, and the evolution of each dislocation segment is computed using a mobility law, relating nodal velocities to nodal forces associated with  $\sigma^d$  induced by a dislocation segment. The nodal force is an essential ingredient and typically expressed in the following form through a Peach-Koehler expression [231],

$$\mathbf{F} = (\sigma^d \cdot \mathbf{b}) \times \xi \quad (78)$$

where  $\xi$  is the unit tangent of the dislocation segment,  $\mathbf{b}$  is the Burgers vector, and  $\times$  is the vector product. In Gu and El-Awady [226], a set of virtual dislocation nodes are introduced based on the continuum H distribution, schematically shown in Fig. 31. The nodal force  $\mathbf{F}^{H,12}$  resulting from a H-induced stress field  $\sigma^{H,12}$  at a particular virtual H-related node  $x_4$  (see Fig. 31) on the dislocation segment bounded by nodes  $x_3$  and  $x_4$  is described as,

$$\mathbf{F}^{H,12} = \int_0^L \frac{1}{L} \left[ \sigma^{H,12} \left( \left( 1 - \frac{1}{L} \right) \mathbf{x}_3 + \frac{1}{L} \mathbf{x}_4 \right) \cdot \mathbf{b}_{43} \right] \times \xi dL \quad (79)$$

where  $L = |x_4 - x_3|$ ,  $\xi = (x_4 - x_3)/L$  and  $\mathbf{b}_{43}$  is the Burgers vector corresponding to a virtual dislocation segment. The total nodal force at any dislocation node is the sum of dislocation nodal force, nodal force related to virtual H nodes, external force, and force term associated with dislocation core energy. Gu and El-Awady [226] successfully quantified the effect of different H concentrations on the dynamics of a glide dislocation and an array of parallel edge dislocations employing the 3D DDD framework. Their results unveiled an H elastic shielding

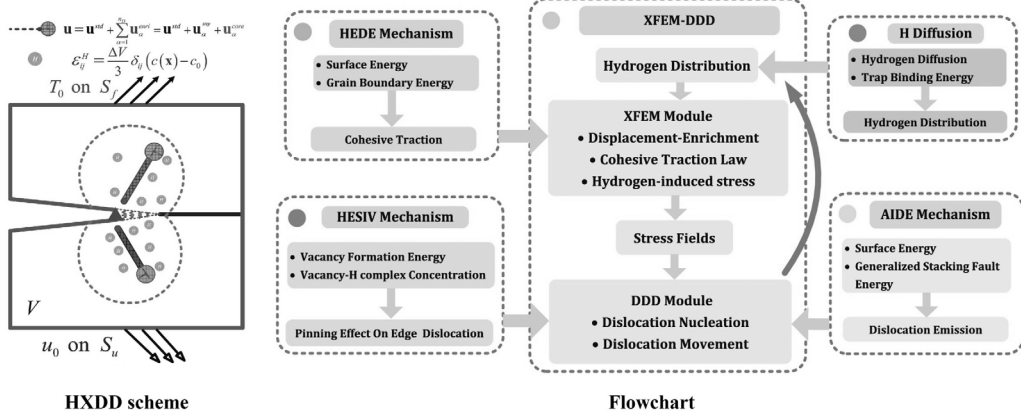


Fig. 32. Visual illustration and flowchart of the H-XFEM-based DDD unified scheme (HXDD) [223].

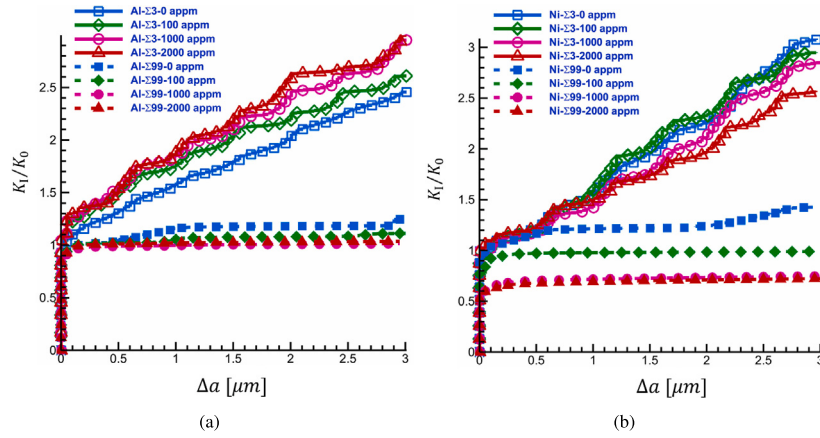


Fig. 33. Normalized SIF ( $K_I/K_0$ ) as a function of crack extension  $\Delta a$  along twin  $\Sigma 3$  and high angle grain boundaries  $\Sigma 99$  for (a) Al, and (b) Ni [223].

(ES) effect akin to experimental observations but primarily observed at high H concentrations.

An XFEM-based DD (HXDD) approach is one of the recent applications of DDD simulations, which allows numerical capabilities to simulate multiple-dislocation emissions and their dynamic evolution, effectively capturing micro-plasticity [228,232]. XFEM is a numerical approach that extends the capabilities of standard FEM to model discontinuities such as cracks independent of the finite element mesh structure, thereby avoiding the need for re-meshing during crack growth [233]. The analogy between the slip plane of dislocations and crack planes allows the dislocation core to be conceptually linked to a crack-tip. XFEM uses discontinuous enrichment functions to capture displacement fields while ensuring the partition of unity of shape functions [234,235]. Within the HXDD scheme, dislocations are treated as displacement discontinuity, where dislocation-core enriched XFEM captures dislocation-interface interactions, including grain boundaries, phase interfaces, particles, voids, and cracks.

To investigate H-induced intergranular fracture behaviors in aluminum (Al) and nickel (Ni), Liang et al. [223] employed an atomistic-informed HXDD framework to quantitatively capture four common HE mechanisms, i.e., HEDE, AIDE, HESIV, and ES. Fig. 32 illustrates the HXDD unified scheme proposed in Liang et al. [223] and its detailed flowchart for simulating H-induced fracture propagation along grain boundaries influenced by dislocations and solute H, considered as a spherical inclusion. Contrary to Gu and El-Awady [226], the H-induced stress field due to solute H is computed using FEM, where the dilatational eigen-strain is integrated over the entire domain. A fast diffusion case is considered from Gu and El-Awady [226], where the H lattice concentration is assumed to be in equilibrium with trapped

H concentration, considering Oriani's equilibrium. The lattice H occupancy is computed using Eq. (76). To simulate HEDE, a cohesive TSL is adopted where exponential binding law describes decohesion along the grain boundaries. The cohesive energy  $\phi_n$  for the interface elements is defined as,

$$\phi_n = \frac{2\gamma_s}{2\gamma_s - \gamma_i} \begin{cases} \text{homogeneous decohesion} \\ \text{interface decohesion} \end{cases} \quad (80)$$

where  $\gamma_s$  is the surface energy of the crack plane and  $\gamma_i$  is the grain boundary energy. The surface energy  $\gamma_s$  is assumed to decrease linearly with the increase in trapped H occupancy  $\theta_T$ . To simulate AIDE, successful dislocation emission is assumed to occur only when the crack-tip energy release rate surpasses the critical value  $G_{ce}$ ,

$$G_{ce} = \frac{0.145\gamma_s + 0.5\gamma_{usf}}{\gamma_{usf}} \quad (81)$$

where  $\gamma_s$  is the surface energy related to surface steps formation and  $\gamma_{usf}$  represents the unstable stacking fault energy related to the shear displacement due to dislocation emissions. The stacking fault energy  $\gamma_{usf}$  is related to trapped H occupancy  $\theta_T$  using DFT and MD simulations. To simulate HESIV, the critical shear stress  $\tau_{cri}$  for a moving dislocation to break through the vacancy-H complexes,

$$\tau_{cri} = \tau_0 + \frac{F_p}{bL} \quad (82)$$

where  $\tau_0$  is the lattice friction stress,  $F_p$  is the pinning force due to vacancy-H complexes or clusters, and  $b$  is the magnitude of the Burgers vector. Fig. 33 presents the fracture resistance curves (normalized SIF ( $K_I/K_0$ ) as a function crack extension  $\Delta a$ ) for the synergistic interplay of different HE mechanisms, such as ES, HEDE, AIDE, and HESIV

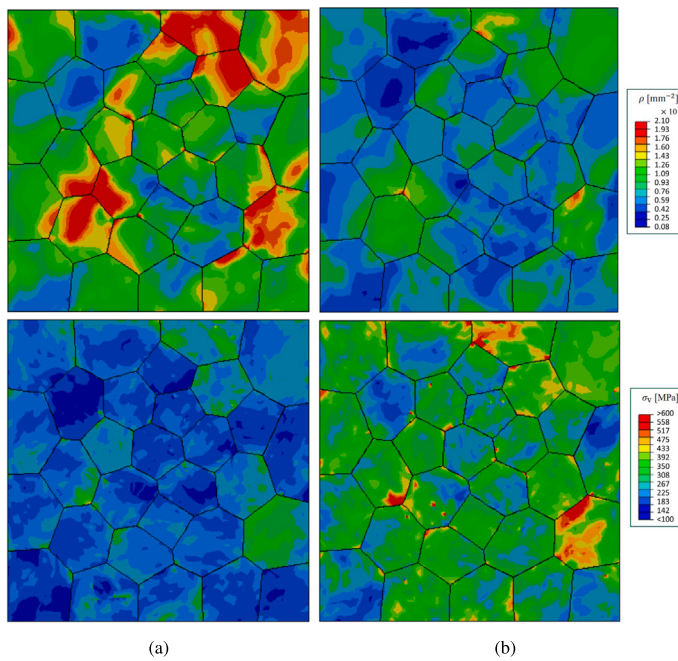


**Fig. 34.** Distribution of total dislocation density  $\rho$  for (a) case 1 and (c) case 2 using a two-way coupled approach in Singh et al. [236].

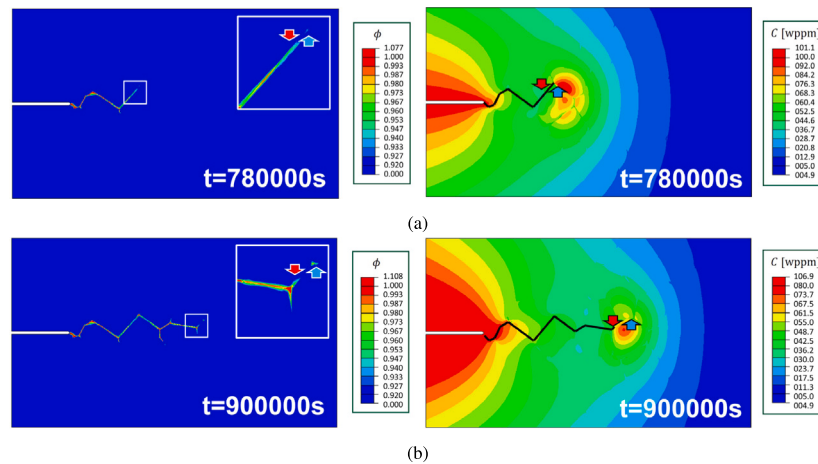


**Fig. 35.** Crack growth and H distribution under the effect of external H at (a)  $t = 780000$  s, and (b)  $t = 920000$  s. The red arrow shows the location of the primary crack-tip, while the blue arrow denotes the location of the secondary crack [117]. (For interpretation of the references to color in this figure legend, the reader is referred to the web version of this article.)

mechanisms along twin  $\Sigma 3$  and high angle  $\Sigma 99$  grain boundaries in Al (see Fig. 33(a)) and Ni (see Fig. 33(b)). Notably, the resistance to crack growth is enhanced with increasing H concentration for Al and decreases for Ni in the case of twin  $\Sigma 3$  grain boundaries, implying AIDE is the dominating HE mechanism. Whereas HEDE controls the crack propagation along the high-angle grain boundary  $\Sigma 99$ , as the fracture resistance decreases for both Al and Ni. Overall, their numerical results revealed that numerous HE mechanisms could coexist and interact in different metals, where the dominant mechanism relies on the kind of grain boundary.

#### 4.4.2. Crystal plasticity simulations

While DDD simulations are less computationally expensive than MD simulations and provide valuable insights into H-dislocation interactions, their applicability is constrained to specific length scales due to the necessity of explicitly modeling individual dislocations [237]. In contrast, CPFE simulations provide a continuum representation of material behavior, thus bridging the length scale gap and enabling the

simulation of larger scales. Furthermore, CPFE models inherently incorporate grain-level effects, such as grain orientation, boundaries, and interactions, which are pivotal for accurately capturing the behavior of polycrystalline materials. This consideration is crucial as grain-level heterogeneity significantly influences mechanical properties. Recent advancements have expanded the scope of CPFE simulations to investigate H-assisted deformation and fracture through various numerical investigations [117,236,238,239].

Singh et al. [236] extended their approach in Kumar and Mahajan [131] (refer to Section 3.5) to a two-way coupling where the H trapping at dislocations influences the critical stresses, dislocation interaction strengths, and dislocation multiplication/annihilations. Fig. 34 illustrates the distribution of total dislocation density and von Mises stress using their two-way approach for different cases. Case 1 (Fig. 34(a)) refers to a HELP-mediated HEDE scenario in which H causes excessive softening with increased dislocation density but not enough elevation in local stresses, thereby necessitating an extra HEDE process for premature failure. Case 2 (Fig. 34(b)) refers to a scenario

caused by the HELP mechanism, resulting in intergranular fracture due to concentrated stress patches and failures around grain boundaries and triple junctions. Li et al. [117] coupled their H diffusion model that incorporates grain boundary character (discussed in Section 3.5) to the PF modeling approach (discussed in Section 4.3.3) to predict the H-assisted cracking process. Fig. 35 illustrates the crack growth and H distribution using their approach under the effect of external H at different time intervals [117]. Notably, crack growth occurs along grain boundaries due to coalescence between primary and secondary cracks that initiate at high-angle grain boundaries and triple junctions.

## 5. Challenges and future perspectives

Despite significant advancements in the coupled analysis of H diffusion, deformation, and fracture, several challenges persist, necessitating further research and innovation. One major hurdle is accurately identifying boundary conditions for H charging or ingress, essential for predicting H-assisted crack growth rates. Quantifying H ingress is particularly complex in gaseous environments (e.g., water vapor) and electrochemical charging in aqueous electrolyte test solutions. Additionally, in real-world conditions, H charging is neither uniform nor constant, fluctuating throughout the equipment's lifetime. These challenges underscore the need for advanced H diffusion models to more accurately resolve the electrochemical diffusion interface or incorporate real-time measurements of H flux from experiments. Some recent developments in predictive electrochemo-mechanical modeling have paved the way for a new generation of models, offering promising avenues for future research to resolve the electrochemistry-diffusion interface during coupled analysis of H-diffusion, deformation, and fracture [77,240].

While CZM and PF modeling approaches have successfully replicated numerous experimental results related to HE, most of these models predominantly focus on the HEDE mechanism. However, HE can manifest through “the plasticity-driven” HE mechanisms such as HELP, HESIV, and AIDE. The scientific community has a growing consensus that multiple HE mechanisms can coexist, adding to the complexity of H-assisted fracture. Some recent continuum-based modeling studies have begun to explore this coexistence, highlighting the necessity for models to capture the dynamic and synergistic effects of multiple HE mechanisms on H diffusion and H-assisted fracture processes [99,174,191,241]. For example, a synergy between HEDE and HELP mechanisms can capture the transition from ductile to brittle-dominated fracture mode, making it essential to develop models that can account for these interactions. However, continuum-scale modeling studies addressing the fracture characteristics associated with HE still lack the incorporation of multiple HE mechanisms simultaneously. Advancements in this area are crucial for understanding the high sensitivity of materials to embrittlement under very low H concentrations — a phenomenon frequently observed in experimental studies but inadequately explained by single-HE-mechanism models. Additionally, many microstructurally sensitive studies have been conducted recently leveraging the capabilities of CPFE simulations, but they are often limited to capturing the interplay between diffusion and deformation, with only some explicitly simulating fracture.

Due to the multi-scale nature of HE, multiscale modeling approaches offer a promising avenue to comprehensively understand these complexities and enable the bottom-up design of materials against HE. Multiscale studies can bridge the gap between H-metal interactions at the atomic, micro, and meso scale to the macroscopic material behavior while considering the effects of microstructural heterogeneities and complex environmental conditions. However, accurately representing the multi-scale nature of HE remains a critical challenge, especially for large components or simulations involving long timescales and numerous loading cycles, and more contributions are required on this topic. Beyond multiscale models, advancements in machine learning algorithms and data analytics offer promising avenues for addressing

the HE problem. Machine learning models can predict mechanical property degradation in the presence of H, identify patterns and correlations in large datasets, and enable more accurate predictions of material behavior under H exposure. By training on extensive datasets, these models can predict H-induced damage in materials, reducing the reliance on purely theoretical approaches. State-of-the-art fracture modeling methods have also proven instrumental in simulating HE and can be integrated with innovative simulation-based paradigms like Digital Twins. This integration can enhance the safety and reliability of infrastructure against HE, offering a comprehensive approach to mitigating its effects.

Finally, the scarcity of high-quality experimental data for validating and refining theoretical and numerical simulations hinders the development of reliable, predictive models. To accurately predict the influence of H on mechanical properties and fracture characteristics of metals and alloys, it is imperative to establish comprehensive databases of tests involving H permeation and H-assisted cracking. These databases should meticulously document testing conditions, H charging methodologies, and measured fracture toughness parameters, facilitating precise comparisons and robust model validations. Comprehensive databases would allow for better benchmarking of models and provide a reference point for future research. Such repositories will provide a firm basis for refining predictive models and advancing our understanding of H-induced degradation in metals and alloys. Collaboration between experimentalists and simulation experts is essential to ensure that experimental data is effectively utilized in model development and validation, ultimately leading to more accurate and reliable predictive tools.

## 6. Summary and conclusions

Coupled modeling approaches are gaining traction among researchers to bridge between theoretical/numerical predictions and empirical observations to address different facets of HE, spanning from H uptake, transport, and distribution within a material media to its impact on mechanical properties and fracture characteristics of various metals and alloys. This comprehensive review sheds light on these advances, covering a broad spectrum of theoretical and numerical models based on coupled modeling methodologies. The discussion starts with a focus on the various advancements made in H diffusion modeling, ranging from fundamental Fickian equations to the most recent developments that involve complex models considering the role of mobile dislocations, crack-tip mechanics, and material microstructure. Notably, SGP theories and CPFE simulations have played a crucial role in these developments, significantly bolstering predictions for H transport and distribution at microstructural and component scales.

In addition to H diffusion modeling, numerous studies have also explored the influence of H on mechanical properties and fracture characteristics of different metals and alloys. These investigations employ coupled deformation-diffusion and deformation-diffusion-fracture methodologies, encompassing a diverse range of theoretical models, continuum-based finite element models, state-of-the-art fracture models, and micro-meso scale physics-based modeling frameworks. Incorporating SGP theories has proven particularly significant, enabling the capture of localized strengthening phenomena and substantially enhancing assessments of crack-tip mechanics and cracking thresholds. PF simulations are noteworthy among fracture modeling applications, which have emerged as promising tools for simulating fractures across different materials while considering multiple physical fields, offering computational efficiency, adaptability, and simplicity.

In recent years, there has been a notable shift in the scale of HE mechanism studies, with an increasing focus on advanced micro-mesoscale investigations utilizing various physics-based frameworks such as DDD and CPFE simulations. DDD simulations, in particular, have emerged as vital contributors, providing insights into H-dislocation interactions that play a pivotal role in elucidating HE mechanisms. Overall, a coupled analysis of H diffusion, deformation,

and fracture holds promise in providing valuable insights into HE and structural integrity evaluations for industrial applications. Moreover, such an approach can enrich our understanding of materials under H-induced conditions at time scales impractical during lab-scale experiments, paving the way for enhanced predictive capabilities in real-world applications and developing materials resistant to HE.

### CRediT authorship contribution statement

**Alok Negi:** Writing – original draft, Visualization, Methodology, Investigation, Formal analysis, Data curation, Conceptualization. **Mohamed Elkhodbia:** Writing – review & editing. **Imad Barsoum:** Writing – review & editing, Supervision, Resources, Project administration, Funding acquisition. **Akram AlFantazi:** Supervision.

### Declaration of competing interest

The authors declare that they have no known competing financial interests or personal relationships that could have appeared to influence the work reported in this paper.

### Acknowledgments

The authors acknowledge the financial support provided by Abu Dhabi National Oil Company (ADNOC), United Arab Emirates under grant no. S.O. 9100000617/KUX 8434000453.

### References

- [1] Rosen MA, Koohi-Fayegh S. The prospects for hydrogen as an energy carrier: an overview of hydrogen energy and hydrogen energy systems. *Energy Ecol Environ* 2016;1:10–29.
- [2] Louthan Jr M, Caskey Jr G. Hydrogen transport and embrittlement in structural metals. *Int J Hydrom Energy* 1976;1(3):291–305.
- [3] Gangloff RP. Hydrogen assisted cracking of high strength alloys. Tech. rep., Aluminum Co of America Alcoa Center Pa Alcoa Technical Center; 2003.
- [4] Johnson WH. II. On some remarkable changes produced in iron and steel by the action of hydrogen and acids. *Proc R Soc Lond* 1875;23(156–163):168–79.
- [5] Rogers HC. Hydrogen embrittlement of metals: Atomic hydrogen from a variety of sources reduces the ductility of many metals. *Science* 1968;159(3819):1057–64.
- [6] Bueno A, Moreira E, Gomes J. Evaluation of stress corrosion cracking and hydrogen embrittlement in an API grade steel. *Eng Fail Anal* 2014;36:423–31.
- [7] Wasim M, Djukic MB, Ngo TD. Influence of hydrogen-enhanced plasticity and decohesion mechanisms of hydrogen embrittlement on the fracture resistance of steel. *Eng Fail Anal* 2021;123:105312.
- [8] Elkhodbia M, Negi A, Mubarak G, Barsoum I, AlFantazi A. Review on sulfide stress cracking in sour service for OCTG and recent advances in modeling of hydrogen-assisted fracture. *Geoenrgy Sci Eng* 2023;212174.
- [9] Mubarak G, Verma C, Mazumder MA, Barsoum I, Alfantazi A. Corrosion inhibition of P110 carbon steel useful for casing and tubing applications in 3.5% NaCl solution using quaternary ammonium-based copolymers. *J Mol Liq* 2024;402:124691.
- [10] Tian H, Wang X, Cui Z, Lu Q, Wang L, Lei L, Li Y, Zhang D. Electrochemical corrosion, hydrogen permeation and stress corrosion cracking behavior of E690 steel in thiosulfate-containing artificial seawater. *Corros Sci* 2018;144:145–62.
- [11] Nagumo M, et al. Fundamentals of hydrogen embrittlement, vol. 921, Springer; 2016.
- [12] Barrera O, Bombac D, Chen Y, Daff T, Galindo-Nava E, Gong P, Haley D, Horton R, Katsarov I, Kermode J, et al. Understanding and mitigating hydrogen embrittlement of steels: a review of experimental, modelling and design progress from atomistic to continuum. *J Mater Sci* 2018;53(9):6251–90.
- [13] Djukic MB, Bakic GM, Zeravcic VS, Sedmak A, Rajicic B. The synergistic action and interplay of hydrogen embrittlement mechanisms in steels and iron: Localized plasticity and decohesion. *Eng Fract Mech* 2019;216:106528.
- [14] Oriani R. Hydrogen embrittlement of steels. *Ann Rev Mater Sci* 1978;8(1):327–57.
- [15] Elkhodbia M, Mubarak G, Gadala I, Barsoum I, AlFantazi A, Al Tamimi A. Experimental and computational failure analysis of hydrogen embrittled steel cords in a reinforced thermoplastic composite pipe. *Eng Fail Anal* 2024;107962.
- [16] Gangloff RP, Somerday BP. Gaseous hydrogen embrittlement of materials in energy technologies: mechanisms, modelling and future developments. Elsevier; 2012.
- [17] Djukic MB, Bakic GM, Zeravcic VS, Sedmak A, Rajicic B. Hydrogen embrittlement of industrial components: prediction, prevention, and models. *Corrosion* 2016;72(7):943–61.
- [18] Martin ML, Dadvania M, Nagao A, Wang S, Sofronis P. Enumeration of the hydrogen-enhanced localized plasticity mechanism for hydrogen embrittlement in structural materials. *Acta Mater* 2019;165:734–50.
- [19] Barrera O, Tarleton E, Tang H, Cocks A. Modelling the coupling between hydrogen diffusion and the mechanical behaviour of metals. *Comput Mater Sci* 2016;122:219–28.
- [20] Birnbaum H. Hydrogen effects on deformation and fracture: science and sociology. *MRS Bull* 2003;28(7):479–85.
- [21] Gerberich W, Stauffer D, Sofronis P. A coexistent view of hydrogen effects on mechanical behavior of crystals: HELP and HEDE. In: Proceedings of the 2008 international hydrogen conference-effects of hydrogen on materials. 2009, p. 38–45.
- [22] Neeraj T, Srinivasan R, Li J. Hydrogen embrittlement of ferritic steels: Observations on deformation microstructure, nanoscale dimples and failure by nanovoiding. *Acta Mater* 2012;60(13–14):5160–71.
- [23] Martin ML, Connolly MJ, DelRio FW, Slifka AJ. Hydrogen embrittlement in ferritic steels. *Appl Phys Rev* 2020;7(4).
- [24] Martin ML, Sofronis P. Hydrogen-induced cracking and blistering in steels: A review. *J Nat Gas Sci Eng* 2022;101:104547.
- [25] Lynch S. Progress towards understanding mechanisms of hydrogen embrittlement and stress corrosion cracking. In: CORROSION 2007. OnePetro; 2007.
- [26] Liu J, Zhao M, Rong L. Overview of hydrogen-resistant alloys for high-pressure hydrogen environment: on the hydrogen energy structural materials. *Clean Energy* 2023;7(1):99–115.
- [27] Pei LB. The effect of occluded hydrogen on the tensile strength of iron. *Proc R Soc Lond Ser A* 1926;112(760):182–95.
- [28] Vehoff H, Neumann P. Crack propagation and cleavage initiation in Fe-2.6%-Si single crystals under controlled plastic crack tip opening rate in various gaseous environments. *Acta Metall* 1980;28(3):265–72.
- [29] Hoagland R, Heinisch H. An atomic simulation of the influence of hydrogen on the fracture behavior of nickel. *J Mater Res* 1992;7(8):2080–8.
- [30] Martin M, Somerday B, Ritchie R, Sofronis P, Robertson I. Hydrogen-induced intergranular failure in nickel revisited. *Acta Mater* 2012;60(6–7):2739–45.
- [31] Wei X, Dong C, Chen Z, Xiao K, Li X. The effect of hydrogen on the evolution of intergranular cracking: a cross-scale study using first-principles and cohesive finite element methods. *RSC Adv* 2016;6(33):27282–92.
- [32] Li X, Zhang J, Fu Q, Song X, Shen S, Li Q. A comparative study of hydrogen embrittlement of 20SiMn2CrNiMo, PSB1080 and PH13-8Mo high strength steels. *Mater Sci Eng A* 2018;724:518–28.
- [33] Beachem CD. A new model for hydrogen-assisted cracking (hydrogen “embrittlement”). *Metall Mater Trans B* 1972;3:441–55.
- [34] Birnbaum HK, Sofronis P. Hydrogen-enhanced localized plasticity—a mechanism for hydrogen-related fracture. *Mater Sci Eng A* 1994;176(1–2):191–202.
- [35] Bond G, Robertson I, Birnbaum H. The influence of hydrogen on deformation and fracture processes in high-strength aluminum alloys. *Acta Metall* 1987;35(9):2289–96.
- [36] Ferreira P, Robertson I, Birnbaum H. Hydrogen effects on the interaction between dislocations. *Acta Mater* 1998;46(5):1749–57.
- [37] Sofronis P, Birnbaum HK. Mechanics of the hydrogen-dislocation-impurity interactions—I. Increasing shear modulus. *J Mech Phys Solids* 1995;43(1):49–90.
- [38] Tabata T, Birnbaum H. Direct observations of the effect of hydrogen on the behavior of dislocations in iron. *Scr Metall* 1983;17(7):947–50.
- [39] Sofronis P, Robertson I. Transmission electron microscopy observations and micromechanical/continuum models for the effect of hydrogen on the mechanical behaviour of metals. *Phil Mag A* 2002;82(17–18):3405–13.
- [40] Lynch S. A fractographic study of hydrogen-assisted cracking and liquid-metal embrittlement in nickel. *J Mater Sci* 1986;21:692–704.
- [41] Tehranchi A, Curtin W. Atomistic study of hydrogen embrittlement of grain boundaries in nickel: I. Fracture. *J Mech Phys Solids* 2017;101:150–65.
- [42] Pundt A, Kirchheim R. Hydrogen in metals: microstructural aspects. *Annu Rev Mater Res* 2006;36:555–608.
- [43] Kuk Y, Silverman P, Nguyen H. Adsorbate-induced reconstruction in the Ni (110)-H system. *Phys Rev Lett* 1987;59(13):1452.
- [44] Song J, Curtin W. Atomic mechanism and prediction of hydrogen embrittlement in iron. *Nat Mater* 2013;12(2):145–51.
- [45] Lynch S. Environmentally assisted cracking: Overview of evidence for an adsorption-induced localised-slip process. *Acta Metall* 1988;36(10):2639–61.
- [46] Nagumo M, Nakamura M, Takai K. Hydrogen thermal desorption relevant to delayed-fracture susceptibility of high-strength steels. *Metall Mater Trans A* 2001;32:339–47.
- [47] Nagumo M. Hydrogen related failure of steels—a new aspect. *Mater Sci Technol* 2004;20(8):940–50.
- [48] Kirchheim R. Reducing grain boundary, dislocation line and vacancy formation energies by solute segregation. I. Theoretical background. *Acta Mater* 2007;55(15):5129–38.

- [49] Sakaki K, Kawase T, Hirato M, Mizuno M, Araki H, Shirai Y, Nagumo M. The effect of hydrogen on vacancy generation in iron by plastic deformation. *Scr Mater* 2006;55(11):1031–4.
- [50] Wang S, Martin ML, Sofronis P, Ohnuki S, Hashimoto N, Robertson IM. Hydrogen-induced intergranular failure of iron. *Acta Mater* 2014;69:275–82.
- [51] Martin M, Robertson I, Sofronis P. Interpreting hydrogen-induced fracture surfaces in terms of deformation processes: A new approach. *Acta Mater* 2011;59(9):3680–7.
- [52] Michler T, Naumann J. Coatings to reduce hydrogen environment embrittlement of 304 austenitic stainless steel. *Surf Coat Technol* 2009;203(13):1819–28.
- [53] Li X, Ma X, Zhang J, Akiyama E, Wang Y, Song X. Review of hydrogen embrittlement in metals: Hydrogen diffusion, hydrogen characterization, hydrogen embrittlement mechanism and prevention. *Acta Metall Sin (Engl Lett)* 2020;33:759–73.
- [54] Jemblie L, Olden V, Akselsen OM. A review of cohesive zone modelling as an approach for numerically assessing hydrogen embrittlement of steel structures. *Phil Trans R Soc A* 2017;375(2098):20160411.
- [55] Sofronis P, McMeeking RM. Numerical analysis of hydrogen transport near a blunting crack tip. *J Mech Phys Solids* 1989;37(3):317–50.
- [56] Krom AH, Koers RW, Bakker A. Hydrogen transport near a blunting crack tip. *J Mech Phys Solids* 1999;47(4):971–92.
- [57] Taha A, Sofronis P. A micromechanics approach to the study of hydrogen transport and embrittlement. *Eng Fract Mech* 2001;68(6):803–37.
- [58] Hirth JP. Effects of hydrogen on the properties of iron and steel. *Metall Trans A* 1980;11:861–90.
- [59] Kiuchi K, McLellan R. The solubility and diffusivity of hydrogen in well-annealed and deformed iron. In: Perspectives in hydrogen in metals. Elsevier; 1986, p. 29–52.
- [60] Jemblie L, Olden V, Akselsen OM. A coupled diffusion and cohesive zone modelling approach for numerically assessing hydrogen embrittlement of steel structures. *Int J Hydrol Energy* 2017;42(16):11980–95.
- [61] Choo W, Lee J-Y. Thermal analysis of trapped hydrogen in pure iron. *Metall Trans A* 1982;13:135–40.
- [62] Pressouyre G, Bernstein I. A quantitative analysis of hydrogen trapping. *Metall Trans A* 1978;9:1571–80.
- [63] Thomas G. Hydrogen trapping in FCC metals. Tech. rep, Sandia National Labs., Livermore, CA (USA); 1980.
- [64] Yagodzinskyy Y, Ivanchenko M, Hänninen H. Hydrogen-dislocation interaction in austenitic stainless steel studied with mechanical loss spectroscopy. *Solid State Phenomena* 2012;184:227–32.
- [65] Novak P, Yuan R, Somerday B, Sofronis P, Ritchie R. A statistical, physical-based, micro-mechanical model of hydrogen-induced intergranular fracture in steel. *J Mech Phys Solids* 2010;58(2):206–26.
- [66] De Oliveira CP, Aucouturier M, Lacombe P. Hydrogen trapping in BCC Fe-Cr alloys (7–9.4 wt% Cr) as studied by microautoradiography—Contribution of carbon-hydrogen interaction—Consequences on hydrogen cracking. *Corrosion* 1980;36(2):53–9.
- [67] Li X, Zhang J, Shen S, Wang Y, Song X. Effect of tempering temperature and inclusions on hydrogen-assisted fracture behaviors of a low alloy steel. *Mater Sci Eng A* 2017;682:359–69.
- [68] Hong G-W, Lee J-Y. The interaction of hydrogen and the cementite-ferrite interface in carbon steel. *J Mater Sci* 1983;18:271–7.
- [69] Zhao J, Jiang Z, Lee CS. Effects of tungsten on the hydrogen embrittlement behaviour of microalloyed steels. *Corros Sci* 2014;82:380–91.
- [70] Chun YS, Kim JS, Park K-T, Lee Y-K, Lee CS. Role of  $\epsilon$  martensite in tensile properties and hydrogen degradation of high-Mn steels. *Mater Sci Eng A* 2012;533:87–95.
- [71] Beele J, Johnson R. Vacancy clusters in  $\alpha$ -iron. *Phys Rev* 1967;156(3):677.
- [72] Maisonneuve J, Oda T, Tanaka S. Molecular statics study of hydrogen isotope trapping in bcc-iron vacancy clusters. *Fusion Sci Technol* 2011;60(4):1507–10.
- [73] Hayward E, Fu C-C. Interplay between hydrogen and vacancies in  $\alpha$ -Fe. *Phys Rev B* 2013;87(17):174103.
- [74] McNabb A, Foster P. A new analysis of diffusion of hydrogen in iron and ferritic steels. *Trans Metall Soc AIME* 1963;227(3):618.
- [75] Oriani RA. The diffusion and trapping of hydrogen in steel. *Acta Metall* 1970;18(1):147–57.
- [76] Drexler A, Depover T, Leitner S, Verbeken K, Ecker W. Microstructural based hydrogen diffusion and trapping models applied to Fe-CX alloys. *J Alloys Compd* 2020;826:154057.
- [77] Martínez-Pañeda E, Díaz A, Wright L, Turnbull A. Generalised boundary conditions for hydrogen transport at crack tips. *Corros Sci* 2020;173:108698.
- [78] Charles Y, Mougenot J, Gaspérini M. Effect of transient trapping on hydrogen transport near a blunting crack tip. *Int J Hydrol Energy* 2021;46(18):10995–1003.
- [79] Krom AH, Bakker A. Hydrogen trapping models in steel. *Metall Mater Trans B* 2000;31:1475–82.
- [80] Johnson HH. Hydrogen in iron. 1988.
- [81] Turnbull A. Modelling of environment assisted cracking. *Corros Sci* 1993;34(6):921–60.
- [82] Bombac D, Katsarov I, Pashov D, Paxton A. Theoretical evaluation of the role of crystal defects on local equilibrium and effective diffusivity of hydrogen in iron. *Mater Sci Technol* 2017;33(13):1505–14.
- [83] Kunnick A, Johnson H. Deep trapping states for hydrogen in deformed iron. *Acta Metall* 1980;28(1):33–9.
- [84] Huang H, Shaw W. Hydrogen embrittlement interactions in cold-worked steel. *Corrosion* 1995;51(1):30–6.
- [85] Colombo C, García AZ, Belzunce J, Pariente IF. Sensitivity to hydrogen embrittlement of AISI 4140 steel: A numerical study on fracture toughness. *Theor Appl Fract Mech* 2020;110:102810.
- [86] Wang Y, Wu X, Zhou Z, Li X. Numerical analysis of hydrogen transport into a steel after shot peening. *Results Phys* 2018;11:5–16.
- [87] Silverstein R, Eliezer D, Tal-Gutelmacher E. Hydrogen trapping in alloys studied by thermal desorption spectrometry. *J Alloys Compd* 2018;747:511–22.
- [88] Dadfarnia M, Sofronis P, Neeraj T. Hydrogen interaction with multiple traps: can it be used to mitigate embrittlement? *Int J Hydrol Energy* 2011;36(16):10141–8.
- [89] Lee S-M, Lee J-Y. The trapping and transport phenomena of hydrogen in nickel. *Metall Trans A* 1986;17:181–7.
- [90] Hondros E, Seah M. The theory of grain boundary segregation in terms of surface adsorption analogues. *Metall Trans A* 1977;8(9):1363–71.
- [91] Serebrinsky S, Carter E, Ortiz M. A quantum-mechanically informed continuum model of hydrogen embrittlement. *J Mech Phys Solids* 2004;52(10):2403–30.
- [92] Martínez-Pañeda E, Golahmar A, Niordson CF. A phase field formulation for hydrogen assisted cracking. *Comput Methods Appl Mech Engrg* 2018;342:742–61.
- [93] McLean D, Maradudin A. Grain boundaries in metals. 1958.
- [94] Lejcek P. Grain boundary segregation in metals, vol. 136, Springer Science & Business Media; 2010.
- [95] Martin ML, Fenske JA, Liu GS, Sofronis P, Robertson IM. On the formation and nature of quasi-cleavage fracture surfaces in hydrogen embrittled steels. *Acta Mater* 2011;59(4):1601–6.
- [96] Nagao A, Smith CD, Dadfarnia M, Sofronis P, Robertson IM. The role of hydrogen in hydrogen embrittlement fracture of lath martensitic steel. *Acta Mater* 2012;60(13–14):5182–9.
- [97] Lufrano J, Sofronis P. Enhanced hydrogen concentrations ahead of rounded notches and cracks—competition between plastic strain and hydrostatic stress. *Acta Mater* 1998;46(5):1519–26.
- [98] Sofronis P, Liang Y, Aravas N. Hydrogen induced shear localization of the plastic flow in metals and alloys. *Eur J Mech A Solids* 2001;20(6):857–72.
- [99] Huang C, Gao X. Phase field modeling of hydrogen embrittlement. *Int J Hydrol Energy* 2020;45(38):20053–68.
- [100] Lufrano J, Sofronis P, Symons D. Hydrogen transport and large strain elastoplasticity near a notch in alloy X-750. *Eng Fract Mech* 1998;59(6):827–45.
- [101] Tien J, Thompson AW, Bernstein I, Richards RJ. Hydrogen transport by dislocations. *Metall Trans A* 1976;7:821–9.
- [102] McLellan RB. Thermodynamics and diffusion behavior of interstitial solute atoms in non-perfect solvent crystals. *Acta Metall* 1979;27(10):1655–63.
- [103] Di Leo CV, Anand L. Hydrogen in metals: a coupled theory for species diffusion and large elastic-plastic deformations. *Int J Plast* 2013;43:42–69.
- [104] Duda FP, Ciabronetti A, Toro S, Huespe AE. A phase-field model for solute-assisted brittle fracture in elastic-plastic solids. *Int J Plast* 2018;102:16–40.
- [105] Wu J-Y, Mandal TK, Nguyen VP. A phase-field regularized cohesive zone model for hydrogen assisted cracking. *Comput Methods Appl Mech Engrg* 2020;358:112614.
- [106] Isfandbod M, Martínez-Pañeda E. A mechanism-based multi-trap phase field model for hydrogen assisted fracture. *Int J Plast* 2021;144:103044.
- [107] Martínez-Pañeda E, del Busto S, Niordson CF, Betegón C. Strain gradient plasticity modeling of hydrogen diffusion to the crack tip. *Int J Hydrol Energy* 2016;41(24):10265–74.
- [108] Díaz A, Alegre J, Cuesta I. Coupled hydrogen diffusion simulation using a heat transfer analogy. *Int J Mech Sci* 2016;115:360–9.
- [109] Anand L, Mao Y, Talamini B. On modeling fracture of ferritic steels due to hydrogen embrittlement. *J Mech Phys Solids* 2019;122:280–314.
- [110] Elmukashfi E, Tarleton E, Cocks AC. A modelling framework for coupled hydrogen diffusion and mechanical behaviour of engineering components. *Comput Mech* 2020;66(1):189–220.
- [111] Anand L. A thermo-mechanically-coupled theory accounting for hydrogen diffusion and large elastic-viscoplastic deformations of metals. *Int J Solids Struct* 2011;48(6):962–71.
- [112] Oriani R, Josephic P. Equilibrium aspects of hydrogen-induced cracking of steels. *Acta Metall* 1974;22(9):1065–74.
- [113] Martínez-Pañeda E, Niordson CF, Gangloff RP. Strain gradient plasticity-based modeling of hydrogen environment assisted cracking. *Acta Mater* 2016;117:321–32.
- [114] Fleck N, Hutchinson J. A reformulation of strain gradient plasticity. *J Mech Phys Solids* 2001;49(10):2245–71.
- [115] Gudmundson P. A unified treatment of strain gradient plasticity. *J Mech Phys Solids* 2004;52(6):1379–406.

- [116] Hussein A, Krom AH, Dey P, Sumardianto GK, Moulton OA, Walters CL. The effect of hydrogen content and yield strength on the distribution of hydrogen in steel: a diffusion coupled micromechanical FEM study. *Acta Mater* 2021;209:116799.
- [117] Li K, Tang B, Zhang M, Zhao L, Liu X, Fan J, Li J. A hydrogen diffusion model considering grain boundary characters based on crystal plasticity framework. *Int J Plast* 2023;103740.
- [118] Koyama M, Yamasaki D, Nagashima T, Tasan CC, Tsuzaki K. In situ observations of silver-decoration evolution under hydrogen permeation: Effects of grain boundary misorientation on hydrogen flux in pure iron. *Scr Mater* 2017;129:48–51.
- [119] Ma Z, Xiong X, Zhang L, Zhang Z, Yan Y, Su Y. Experimental study on the diffusion of hydrogen along individual grain boundaries in nickel. *Electrochim Commun* 2018;92:24–8.
- [120] Díaz A, Zafra A, Martínez-Pañeda E, Alegre J, Belzunce J, Cuesta II. Simulation of hydrogen permeation through pure iron for trapping and surface phenomena characterisation. *Theor Appl Fract Mech* 2020;110:102818.
- [121] Mai HL, Cui X-Y, Scheiber D, Romaner L, Ringer SP. An understanding of hydrogen embrittlement in nickel grain boundaries from first principles. *Mater Des* 2021;212:110283.
- [122] Ilin DN, Saintier N, Olive J-M, Abgrall R, Aubert I. Simulation of hydrogen diffusion affected by stress-strain heterogeneity in polycrystalline stainless steel. *Int J Hydrol Energy* 2014;39(5):2418–22.
- [123] Abdolvand H. Progressive modelling and experimentation of hydrogen diffusion and precipitation in anisotropic polycrystals. *Int J Plast* 2019;116:39–61.
- [124] Hassan HU, Govind K, Hartmaier A. Micromechanical modelling of coupled crystal plasticity and hydrogen diffusion. *Phil Mag* 2019;99(1):92–115.
- [125] Tondro A, Abdolvand H. On the effects of texture and microstructure on hydrogen transport towards notch tips: A CPFE study. *Int J Plast* 2022;152:103234.
- [126] Park J, Shin G, Kim H-J, Kim K, Yoon SC, Sohn SS, Lee M-G. A continuum scale chemo-mechanical model for multi-trap hydrogen transport in deformed polycrystalline metals. *Int J Plast* 2024;173:103890.
- [127] Rice JR. Inelastic constitutive relations for solids: an internal-variable theory and its application to metal plasticity. *J Mech Phys Solids* 1971;19(6):433–55.
- [128] Hutchinson JW. Bounds and self-consistent estimates for creep of polycrystalline materials. *Proc R Soc A* 1976;348(1652):101–27.
- [129] Peirce D, Asaro RJ, Needleman A. Material rate dependence and localized deformation in crystalline solids. *Acta Metall* 1983;31(12):1951–76.
- [130] Franciosi P. The concepts of latent hardening and strain hardening in metallic single crystals. *Acta Metall* 1985;33(9):1601–12.
- [131] Kumar R, Mahajan DK. Hydrogen distribution in metallic polycrystals with deformation. *J Mech Phys Solids* 2020;135:103776.
- [132] Yuan S, Zhu Y, Huang M, Liang S, Li Z. Dislocation-density based crystal plasticity model with hydrogen-enhanced localized plasticity in polycrystalline face-centered cubic metals. *Mech Mater* 2020;148:103472.
- [133] Mecking H, Kocks U. Kinetics of flow and strain-hardening. *Acta Metall* 1981;29(11):1865–75.
- [134] Orowan E. Problems of plastic gliding. *Proc Phys Soc* 1940;52(1):8.
- [135] Taylor GI. The mechanism of plastic deformation of crystals. Part I.—Theoretical. *Proc R Soc Lond Ser A* 1934;145(855):362–87.
- [136] Franciosi P, Zaoui A. Multislip tests on copper crystals: a junctions hardening effect. *Acta Metall* 1982;30(12):2141–51.
- [137] Jothi S, Croft T, Brown S. Coupled macroscale-microscale model for hydrogen embrittlement in polycrystalline materials. *Int J Hydrol Energy* 2015;40(6):2882–9.
- [138] Jothi S, Croft T, Wright L, Turnbull A, Brown S. Multi-phase modelling of intergranular hydrogen segregation/trapping for hydrogen embrittlement. *Int J Hydrol Energy* 2015;40(43):15105–23.
- [139] Choo W, Lee JY. Effect of cold working on the hydrogen trapping phenomena in pure iron. *Metall Trans A* 1983;14:1299–305.
- [140] Hirth J, Johnson H. On the transport of hydrogen by dislocations. In: Atomistics of fracture. Springer; 1983, p. 771–87.
- [141] Frankel G, Latanision R. Hydrogen transport during deformation in nickel: Part II. Single crystal nickel. *Metall Trans A* 1986;17:869–75.
- [142] Pu S, Ooi S. Hydrogen transport by dislocation movement in austenitic steel. *Mater Sci Eng A* 2019;761:138059.
- [143] Dadfarnia M, Martin ML, Nagao A, Sofronis P, Robertson IM. Modeling hydrogen transport by dislocations. *J Mech Phys Solids* 2015;78:511–25.
- [144] Charles Y, Mougenot J, Gasperini M. Modeling hydrogen dragging by mobile dislocations in finite element simulations. *Int J Hydrol Energy* 2022;47(28):13746–61.
- [145] Yuan S, Zhu Y, Zhao L, Liang S, Huang M, Li Z. Key role of plastic strain gradient in hydrogen transport in polycrystalline materials. *Int J Plast* 2022;158:103409.
- [146] Zirkle T, Costello L, Zhu T, McDowell DL. Modeling dislocation-mediated hydrogen transport and trapping in face-centered cubic metals. *J Eng Mater Technol* 2022;144(1):011005.
- [147] Moro I, Briottet L, Lemoine P, Andrieu E, Blanc C, Odemer G. Hydrogen embrittlement susceptibility of a high strength steel X80. *Mater Sci Eng A* 2010;527(27–28):7252–60.
- [148] Mubarak G, Verma C, Barsoum I, Alfantazi A, Rhee KY. Internal corrosion in oil and gas wells during casings and tubing: Challenges and opportunities of corrosion inhibitors. *J Taiwan Inst Chem Eng* 2023;150:105027.
- [149] Sieverts A, Krumbhaar W. On the solubility of gases in metals and alloys. *Rep German Chem Soc* 1910;43(1):893–900.
- [150] Alvaro A, Olden V, Akselsen OM. 3D cohesive modelling of hydrogen embrittlement in the heat affected zone of an X70 pipeline steel—Part II. *Int J Hydrol Energy* 2014;39(7):3528–41.
- [151] Díaz A, Alegre J, Cuesta I. Numerical simulation of hydrogen embrittlement and local triaxiality effects in notched specimens. *Theor Appl Fract Mech* 2017;90:294–302.
- [152] Das T, Legrand E, Brahimi SV, Song J, Yue S. Evaluation of material susceptibility to hydrogen embrittlement (HE): An approach based on experimental and finite element (FE) analyses. *Eng Fract Mech* 2020;224:106714.
- [153] Krom A, Bakker A, Koers R. Modelling hydrogen-induced cracking in steel using a coupled diffusion stress finite element analysis. *Int J Press Vessels Pip* 1997;72(2):139–47.
- [154] Akhurst K, Baker T. The threshold stress intensity for hydrogen-induced crack growth. *Metall Trans A* 1981;12:1059–70.
- [155] Gerberich W, Lvne T, Chen X, Kaczorowski M. Crack growth from internal hydrogen—Temperature and microstructural effects in 4340 steel. *Metall Trans A* 1988;19:1319–34.
- [156] Nair S, Tien J. A plastic flow induced fracture theory for K iscc. *Metall Trans A* 1985;16:2333–40.
- [157] Lee SL, Unger DJ. A decohesion model of hydrogen assisted cracking. *Eng Fract Mech* 1988;31(4):647–60.
- [158] Unger DJ. A mathematical analysis for impending hydrogen assisted crack propagation. *Eng Fract Mech* 1989;34(3):657–67.
- [159] Huang H, Gerberich WW. Quasi-equilibrium modeling of the toughness transition during semibrittle cleavage. *Acta Metall Mater* 1994;42(3):639–47.
- [160] Gangloff R, Turnbull A. In: Jones RH, Gerberich WW, editors. Modeling environmental effects on crack initiation and propagation. 1986, p. 55.
- [161] Wang J-S. The thermodynamics aspects of hydrogen induced embrittlement. *Eng Fract Mech* 2001;68(6):647–69.
- [162] Liang Y, Sofronis P. Toward a phenomenological description of hydrogen-induced decohesion at particle/matrix interfaces. *J Mech Phys Solids* 2003;51(8):1509–31.
- [163] Jung S-P, Kwon Y, Lee CS, Lee B-J. Influence of hydrogen on the grain boundary crack propagation in bcc iron: A molecular dynamics simulation. *Comput Mater Sci* 2018;149:424–34.
- [164] Nagao A, Dadfarnia M, Somerdøy BP, Sofronis P, Ritchie RO. Hydrogen-enhanced-plasticity mediated decohesion for hydrogen-induced intergranular and “quasi-cleavage” fracture of lath martensitic steels. *J Mech Phys Solids* 2018;112:403–30.
- [165] Wu W, Wang Y, Tao P, Li X, Gong J. Cohesive zone modeling of hydrogen-induced delayed intergranular fracture in high strength steels. *Results Phys* 2018;11:591–8.
- [166] Huang Y, Chen J, Wang Y, Liu W, Wu W, Li X, Yang X. A physically based model predicting the degradation of hydrogen on crack growth critical stress intensity factor of metals. *Metals* 2022;12(9):1441.
- [167] Hirth JP, Rice JR. On the thermodynamics of adsorption at interfaces as it influences decohesion. *Metall Trans A* 1980;11:1501–11.
- [168] Rice JR, Wang J-S. Embrittlement of interfaces by solute segregation. *Mater Sci Eng A* 1989;107:23–40.
- [169] Olden V, Thaulow C, Johnsen R. Modelling of hydrogen diffusion and hydrogen induced cracking in supermartensitic and duplex stainless steels. *Mater & Des* 2008;29(10):1934–48.
- [170] Kharin V. Comments on “computational analysis of geometrical factors affecting experimental data extracted from hydrogen permeation tests: I—consequences of trapping” [int j hydrogen energy 36 (2011) 12644–12652] and “...II—consequences of trapping and an oxide layer” [int j hydrogen energy 37 (2012) 13574–13582], “corrigenda...” to both [int j hydrogen energy 39 (2014) 2430], and on “...III—comparison with experimental results from the literature” [int j hydrogen energy 39 (2014) 1145–1155] with “generalized model of desorption kinetics: Characterization of hydrogen trapping in a homogeneous membrane” [int j hydrogen energy 39 (2014) 8374–8384]. *Int J Hydrol Energy* 2014;39(34):19846–50.
- [171] Miresmaeli R, Ogino M, Nakagawa T, Kanayama H. A coupled elastoplastic-transient hydrogen diffusion analysis to simulate the onset of necking in tension by using the finite element method. *Int J Hydrol Energy* 2010;35(3):1506–14.
- [172] Cui T, Liu P, Gu C. Finite element analysis of hydrogen diffusion/plasticity coupled behaviors of low-alloy ferritic steel at large strain. *Int J Hydrol Energy* 2017;42(31):20324–35.
- [173] Yu H, Olsen JS, Alvaro A, Qiao L, He J, Zhang Z. Hydrogen informed Gurson model for hydrogen embrittlement simulation. *Eng Fract Mech* 2019;217:106542.
- [174] Huang S, Zhang Y, Yang C, Hu H. Fracture strain model for hydrogen embrittlement based on hydrogen enhanced localized plasticity mechanism. *Int J Hydrol Energy* 2020;45(46):25541–54.

- [175] Depraetere R, De Waele W, Hertelé S. Fully-coupled continuum damage model for simulation of plasticity dominated hydrogen embrittlement mechanisms. *Comput Mater Sci* 2021;200:110857.
- [176] Das T, Chakrabarty R, Song J, Yu S. Understanding microstructural influences on hydrogen diffusion characteristics in martensitic steels using finite element analysis (FEA). *Int J Hydrog Energy* 2022;47(2):1343–57.
- [177] Ashby M. The deformation of plastically non-homogeneous materials. *Phil Mag: J Theor Exp Appl Phys* 1970;21(170):399–424.
- [178] Martínez-Pañeda E, Betegón C. Modeling damage and fracture within strain-gradient plasticity. *Int J Solids Struct* 2015;59:208–15.
- [179] Martínez-Pañeda E, Niordson CF. On fracture in finite strain gradient plasticity. *Int J Plast* 2016;80:154–67.
- [180] Gerberich W, Oriani R, Lji M-J, Chen X, Foecke T. The necessity of both plasticity and brittleness in the fracture thresholds of iron. *Phil Mag A* 1991;63(2):363–76.
- [181] Pineau A. Modeling ductile to brittle fracture transition in steels—micromechanical and physical challenges. *Int J Fract* 2008;150:129–56.
- [182] Dugdale DS. Yielding of steel sheets containing slits. *J Mech Phys Solids* 1960;8(2):100–4.
- [183] Barenblatt GI. The mathematical theory of equilibrium cracks in brittle fracture. *Adv Appl Mech* 1962;7(C):55–129.
- [184] Olden V, Thaulow C, Johnsen R, Østby E. Cohesive zone modeling of hydrogen-induced stress cracking in 25% Cr duplex stainless steel. *Scr Mater* 2007;57(7):615–8.
- [185] Olden V, Thaulow C, Johnsen R, Østby E, Berstad T. Application of hydrogen influenced cohesive laws in the prediction of hydrogen induced stress cracking in 25% Cr duplex stainless steel. *Eng Fract Mech* 2008;75(8):2333–51.
- [186] Alvaro A, Jensen IT, Kheradmand N, Løvvik O, Olden V. Hydrogen embrittlement in nickel, visited by first principles modeling, cohesive zone simulation and nanomechanical testing. *Int J Hydrog Energy* 2015;40(47):16892–900.
- [187] Gobbi G, Colombo C, Vergani L. Sensitivity analysis of a 2D cohesive model for hydrogen embrittlement of AISI 4130. *Eng Fract Mech* 2016;167:101–11.
- [188] Yu H, Olsen JS, Olden V, Alvaro A, He J, Zhang Z. Viscous regularization for cohesive zone modeling under constant displacement: An application to hydrogen embrittlement simulation. *Eng Fract Mech* 2016;166:23–42.
- [189] Sedlak M, Alfredsson B, Efsing P. A cohesive element with degradation controlled shape of the traction separation curve for simulating stress corrosion and irradiation cracking. *Eng Fract Mech* 2018;193:172–96.
- [190] Sedlak M, Alfredsson B, Efsing P. A coupled diffusion and cohesive zone model for intergranular stress corrosion cracking in 316L stainless steel exposed to cold work in primary water conditions. *Eng Fract Mech* 2019;217:106543.
- [191] Lin M, Yu H, Ding Y, Olden V, Alvaro A, He J, Zhang Z. Simulation of ductile-to-brittle transition combining complete Gurson model and CZM with application to hydrogen embrittlement. *Eng Fract Mech* 2022;268:108511.
- [192] Lin M, Yu H, Wang X, Wang R, Ding Y, Alvaro A, Olden V, He J, Zhang Z. A microstructure informed and mixed-mode cohesive zone approach to simulating hydrogen embrittlement. *Int J Hydrog Energy* 2022;47(39):17479–93.
- [193] Thomas RL, Scully JR, Gangloff RP. Internal hydrogen embrittlement of ultrahigh-strength AERMET 100 steel. *Mater Mater Trans A* 2003;34(2):327–44.
- [194] Van der Ven A, Ceder G. Impurity-induced van der Waals transition during decohesion. *Phys Rev B* 2003;67(6):060101.
- [195] Jiang D, Carter EA. First principles assessment of ideal fracture energies of materials with mobile impurities: implications for hydrogen embrittlement of metals. *Acta Mater* 2004;52(16):4801–7.
- [196] Alvaro A, Olden V, Akselsen OM. 3D cohesive modelling of hydrogen embrittlement in the heat affected zone of an X70 pipeline steel. *Int J Hydrog Energy* 2013;38(18):7539–49.
- [197] Zhang Z, Thaulow C, Ødegård J. A complete Gurson model approach for ductile fracture. *Eng Fract Mech* 2000;67(2):155–68.
- [198] Xu K, Rana M. Tensile and fracture properties of carbon and low alloy steels in high pressure hydrogen. In: Proceedings of the 2008 international hydrogen conference. 2009, p. 349–56.
- [199] Wang M, Akiyama E, Tsuzaki K. Effect of hydrogen and stress concentration on the notch tensile strength of AISI 4135 steel. *Mater Sci Eng A* 2005;398(1–2):37–46.
- [200] Cervera M, Chiumenti M. Smeared crack approach: back to the original track. *Int J Numer Anal Methods Geomech* 2006;30(12):1173–99.
- [201] De Borst R, Crisfield MA, Remmers JJ, Verhoosel CV. Nonlinear finite element analysis of solids and structures. John Wiley & Sons; 2012.
- [202] Kristensen PK, Niordson CF, Martínez-Pañeda E. A phase field model for elastic-gradient-plastic solids undergoing hydrogen embrittlement. *J Mech Phys Solids* 2020;143:104093.
- [203] Kristensen PK, Niordson CF, Martínez-Pañeda E. Applications of phase field fracture in modelling hydrogen assisted failures. *Theor Appl Fract Mech* 2020;110:102837.
- [204] Fernández-Sousa R, Betegón C, Martínez-Pañeda E. Analysis of the influence of microstructural traps on hydrogen assisted fatigue. *Acta Mater* 2020;199:253–63.
- [205] Dinachandra M, Alankar A. Adaptive finite element modeling of phase-field fracture driven by hydrogen embrittlement. *Comput Methods Appl Mech Engrg* 2022;391:114509.
- [206] Golahmar A, Kristensen PK, Niordson CF, Martínez-Pañeda E. A phase field model for hydrogen-assisted fatigue. *Int J Fatigue* 2022;154:106521.
- [207] Negi A, Barsoum I, AlFantazi A. Predicting sulfide stress cracking in a sour environment: A phase-field finite element study. *Theor Appl Fract Mech* 2023;127:104084.
- [208] Si Z, Yu T, Natarajan S, et al. An adaptive phase-field simulation for hydrogen embrittlement fracture with multi-patch isogeometric method. *Comput Methods Appl Mech Engrg* 2024;418:116539.
- [209] Liu T-R, Aldakheel F, Aliabadi M. Hydrogen assisted cracking using an efficient virtual element scheme. *Comput Methods Appl Mech Engrg* 2024;420:116708.
- [210] Cui C, Bortot P, Ortolani M, Martínez-Pañeda E. Computational predictions of hydrogen-assisted fatigue crack growth. *Int J Hydrog Energy* 2024;72:315–25.
- [211] Valverde-González A, Martínez-Pañeda E, Quintanilla-Corominas A, Reinoso J, Paggi M. Computational modelling of hydrogen assisted fracture in polycrystalline materials. *Int J Hydrog Energy* 2022;47(75):32235–51.
- [212] Sukumar N, Srolovitz D, Baker T, Prevost J-H. Brittle fracture in polycrystalline microstructures with the extended finite element method. *Internat J Numer Methods Engrg* 2003;56(14):2015–37.
- [213] Clayton J, Knap J. Phase field modeling of directional fracture in anisotropic polycrystals. *Comput Mater Sci* 2015;98:158–69.
- [214] Nguyen T-T, Réthoré J, Yvonnet J, Baietto M-C. Multi-phase-field modeling of anisotropic crack propagation for polycrystalline materials. *Comput Mech* 2017;60:289–314.
- [215] Negi A, Singh I, Barsoum I. A gradient-enhanced damage model for anisotropic brittle fracture with interfacial damage in polycrystalline materials. *Eng Fract Mech* 2023;280:109093.
- [216] Hirose Y, Mura T. Growth mechanism of stress corrosion cracking in high strength steel. *Eng Fract Mech* 1984;19(6):1057–67.
- [217] Ran X, Qian S, Zhou J, Xu Z. Crack propagation analysis of hydrogen embrittlement based on peridynamics. *Int J Hydrog Energy* 2022;47(14):9045–57.
- [218] De Meo D, Diyaroglu C, Zhu N, Oterkus E, Siddiq MA. Modelling of stress-corrosion cracking by using peridynamics. *Int J Hydrog Energy* 2016;41(15):6593–609.
- [219] Chen Z, Yang D, Bian H. Peridynamic modeling of crack propagation driven by hydrogen embrittlement. *Eng Fract Mech* 2023;293:109687.
- [220] Chen Z, Bobaru F. Peridynamic modeling of pitting corrosion damage. *J Mech Phys Solids* 2015;78:352–81.
- [221] Van der Giessen E, Needleman A. Discrete dislocation plasticity: a simple planar model. *Modelling Simul Mater Sci Eng* 1995;3(5):689.
- [222] Cleveringa H, Van der Giessen E, Needleman A. A discrete dislocation analysis of mode I crack growth. *J Mech Phys Solids* 2000;48(6–7):1133–57.
- [223] Liang S, Huang M, Zhao L, Zhu Y, Li Z. Effect of multiple hydrogen embrittlement mechanisms on crack propagation behavior of FCC metals: Competition vs. synergy. *Int J Plast* 2021;143:103023.
- [224] Dong L, Wang S, Wu G, Gao J, Zhou X, Wu H-H, Mao X. Application of atomic simulation for studying hydrogen embrittlement phenomena and mechanism in iron-based alloys. *Int J Hydrog Energy* 2022;47(46):20288–309.
- [225] Irani N, Remmers J, Deshpande V. A discrete dislocation analysis of hydrogen-assisted mode-I fracture. *Mech Mater* 2017;105:67–79.
- [226] Gu Y, El-Awady JA. Quantifying the effect of hydrogen on dislocation dynamics: A three-dimensional discrete dislocation dynamics framework. *J Mech Phys Solids* 2018;112:491–507.
- [227] Yu H, Cocke A, Tarleton E. Discrete dislocation plasticity HELPs understand hydrogen effects in bcc materials. *J Mech Phys Solids* 2019;123:41–60.
- [228] Liang S, Zhu Y, Huang M, Li Z. Simulation on crack propagation vs. crack-tip dislocation emission by XFEM-based DDD scheme. *Int J Plast* 2019;114:87–105.
- [229] Lavenstein S, El-Awady JA. Micro-scale fatigue mechanisms in metals: Insights gained from small-scale experiments and discrete dislocation dynamics simulations. *Curr Opin Solid State Mater Sci* 2019;23(5):100765.
- [230] Cai W, Sills R, Barnett D, Nix W. Modeling a distribution of point defects as misfitting inclusions in stressed solids. *J Mech Phys Solids* 2014;66:154–71.
- [231] Gururanga-Lerma B, Balint DS, Dini D, Eakins DE, Sutton AP. A dynamic discrete dislocation plasticity method for the simulation of plastic relaxation under shock loading. *Proc R Soc A* 2013;469(2156):20130141.
- [232] Huang M, Huang S, Liang S, Zhu Y, Li Z. An efficient 2D discrete dislocation Dynamics-XFEM coupling framework and its application to polycrystal plasticity. *Int J Plast* 2020;127:102647.
- [233] Belytschko T, Black T. Elastic crack growth in finite elements with minimal remeshing. *Internat J Numer Methods Engrg* 1999;45(5):601–20.
- [234] Jha A, Sarkar S, Singh I, Mishra B, Singh R, Singh R. A study on the effect of residual stresses on hydride assisted crack in Zr-2.5 Nb pressure tube material using XFEM. *Theor Appl Fract Mech* 2022;121:103536.
- [235] Negi A, Kumar S. A continuous-discontinuous localizing gradient damage framework for failure analysis of quasi-brittle materials. *Comput Methods Appl Mech Engrg* 2022;390:114434.
- [236] Singh V, Kumar R, Charles Y, Mahajan DK. Coupled diffusion-mechanics framework for simulating hydrogen assisted deformation and failure behavior of metals. *Int J Plast* 2022;157:103392.

- [237] Tarleton E. Incorporating hydrogen in mesoscale models. *Comput Mater Sci* 2019;163:282–9.
- [238] Kumar R, Mahajan DK. Modelling of hydrogen-assisted damage at the deforming single crystal crack-tip. *Mech Mater* 2023;178:104557.
- [239] Kumar P, Ludhwani MM, Das S, Gavini V, Kanjrala A, Adlakha I. Effect of hydrogen on plasticity of  $\alpha$ -Fe: A multi-scale assessment. *Int J Plast* 2023;165:103613.
- [240] Hageman T, Martínez-Pañeda E. An electro-chemo-mechanical framework for predicting hydrogen uptake in metals due to aqueous electrolytes. *Corros Sci* 2022;208:110681.
- [241] Yuan S, Zhu Y, Huang M, Zhao L, Liang S, Li Z. A coupled diffusional-mechanical model accounting for hydrogen enhancements of strain-induced dislocations and vacancies. *Mech Mater* 2023;186:104781.